Nuclear Inst. and Methods in Physics Research, A 1022 (2022) 165957

Contents lists available at ScienceDirect

Nuclear Inst. and Methods in Physics Research, A

journal homepage: www.elsevier.com/locate/nima

High-energy per-pixel calibration of timepix pixel detector with laboratory alpha source

Marek Sommer [a,b,*], Carlos Granja [c,**], Satoshi Kodaira [d], Ondřej Ploc [a]

[a] Nuclear Physics Institute of the Czech Academy of Sciences, Řež, Czech Republic
[b] Czech Technical University in Prague, Faculty of Nuclear Sciences and Physical Engineering, Prague 1, 115 19, Czech Republic
[c] Advacam, U Pergamenky 12, 17000 Prague 7, Czech Republic
[d] National Institutes for Quantum and Radiological Science and Technology, Inage, Chiba 263-8555, Japan

ABSTRACT

The spectral response of the pixel detector Timepix at the high per-pixel proportional range is examined and calibrated using a simple technique and alpha particles from a standard laboratory source in air. For the detector used, a Timepix ASIC chip equipped with a 300 μ m thick silicon sensor, the spectral range is newly extended up to about 1750 keV per-pixel. This expands and covers the region above 850 keV per pixel which is described and covered by the existing low-energy calibration. The low-energy calibration uses discrete low-energy gamma rays in the range 5–60 keV and is extrapolated over the linear range up to 850 keV/px. Above this level, the per-pixel spectral response changes. At higher energies it undergoes distortion and saturation. The proportional and monotonic response is observed with regions of varying dependence up to nearly 2 MeV. This high-energy region is covered and described by the newly developed calibration method which Uses an alpha source of common low activity (kBq level). Data are collected within one day of total measuring time. Measurements are performed in air at various source-to-distance positions and several sensor bias settings. The developed method together with suitable setting of the sensor bias, which determines the extent of charge sharing, expands the spectral response of Timepix to high energy-loss particles such as alpha particles and light ions in wide energy range. Results are demonstrated on alpha particles, protons and ^{12}C ions. Resulting spectra of deposited energy and cluster pixel height are correctly calibrated and they reproduce expected values.

1. Introduction, motivation, previous work

The hybrid semiconductor pixel detector Timepix [1] provides high spatial granularity and per-pixel spectral response for broad application in basic and applied research [2–5]. Many applications make use of energy-sensitive measurements such as radiation and particle imaging [6–8], charged particle spectrometry and dosimetry [9–11], spectral-tracking characterization of energetic charged particles [12, 13] in atmospheric cosmic rays [11] and in mixed-radiation fields at accelerator [14] and radiotherapy environments [15,16] as well as in outer space at LEO orbit [17–21].

Measurements of deposited energy [11,22], energy loss [13] and Linear-Energy-Transfer (LET) spectra [23–25] require wide-range energy calibration of the detector at the per-pixel level. The aim is to examine and expand the spectral response range at high energy, improve the energy resolution and keep a low detection threshold (at the level 4 keV per pixel). This combined effort is the subject of this and previous cited work.

The spectral response at the pixel level for the Timepix detector ranges from few keV (e.g., 4 keV for a 300 μm silicon sensor) up to few MeV with varying type of dependence as illustrated in Fig. 1. The per-pixel calibration is standardly performed in the low-energy range i.e., for energies well below 1 MeV per-pixel. In this range, the conventional technique [26] makes use of mono-energetic X rays (XRF) and low-energy gamma rays up to 60 keV. Above this level, the calibration is extrapolated up to about 850 keV. This upper energy range is denoted in this work as low-energy linear cut-off level. It corresponds to the well-described proportional region exhibiting linear dependence. Another technique uses test pulses which can be exploited to examine and calibrate the per-pixel response [27,28] covering the low-energy and partly also the high-energy regions. In an effort to test and calibrate the high-energy region, heavy charged particles have been used namely protons of energy 5 MeV and 8 MeV [29,30] as well as alpha particles from a laboratory radionuclide source [31]. Also energetic heavy ions (400 MeV/u ^{40}Ar ions) [29,30] were used in an attempt to examine and calibrate an even higher-energy region. An overall feature of these techniques is the need for a well-defined radiation source namely in the form of a particle accelerator beam. The emphasis and approach chosen in the present work, is to provide a simplified technique of minimal complexity using a readily available radiation source, a basic setup and simple measurements in air.

The detector instrumentation used namely the semiconductor pixel detector is briefly described in Section 2. Emphasis is given on the spectral registration of the signals registered by charged particles in

* Corresponding author at: Nuclear Physics Institute of the Czech Academy of Sciences, Řež, Czech Republic.
** Corresponding author.
E-mail addresses: sommer@ujf.cas.cz (M. Sommer), carlos.granja@advacam.com (C. Granja).

https://doi.org/10.1016/j.nima.2021.165957
Received 17 August 2021; Received in revised form 13 October 2021; Accepted 20 October 2021
Available online 30 October 2021
0168-9002/

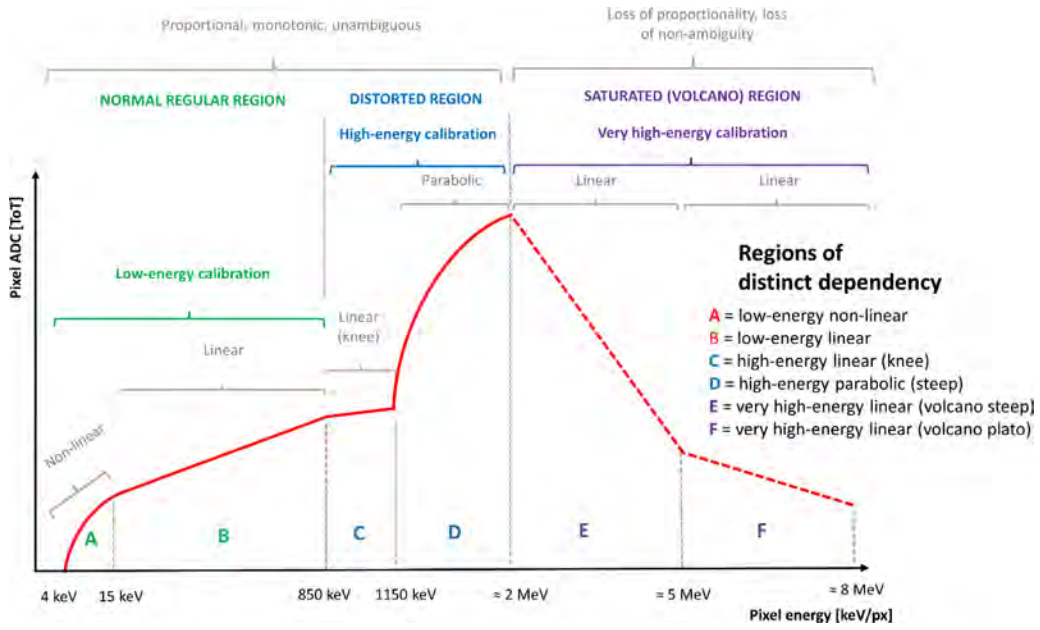

Fig. 1. Illustration of the pixel-level spectral response of Timepix showing (red curve). The pixel energy response (X axis) derived in keV is determined by the registered ToT signal (Y axis). The values of the energy borders between the various segments are approximate. (For interpretation of the references to colour in this figure legend, the reader is referred to the web version of this article.)

the pixelated detector and the spectral response at the pixel level. The effect and suitable use of the bias voltage applied to the semiconductor sensor is described and exploited in this work. Section 3 describes the experimental setup and approach of data acquisition especially in view of the calibration method developed. A tuneable measuring setup is required with the aim of deriving the deposited energy by the alpha particles of energy of few MeV. For this purpose, data were collected for various source-to-detector distances and at several sensor bias voltages.

The procedure of the high-energy calibration is described in Section 4. This reviews the approach and strategy of data processing. Steps include derivation of the large deposited energy by the alpha particles on the detector. This is achieved by selecting events exhibiting limited values of maximal per-pixel energy. This is fulfilled by alpha particles hitting the proximity of the border between pixels. In such case, the large deposited energy is more evenly distributed among two or more pixels. In the next step, events which have large values of registered energy in the central pixel are processed. This is the case of alpha particles hitting the centre of a given pixel, away from the border region with adjacent pixels. The regions of different and distinct proportionality are identified and described. The fitting functions coefficients are calculated together with thresholds and extent of proportionality regions. The upper range of the developed calibration is examined and determined.

The developed calibration is evaluated and tested in Section 5. This is performed on the same data collected for the calibration and also on proton and light ion data. Deposited energy spectra and distributions of maximal per-pixel energy are derived with the new calibration and compared with the previous low-energy calibration. The energy resolution is evaluated and determined. The results of the developed calibration and upper range applicability are also evaluated in terms of resulting LET values for the measured heavy charged particles. Results of the technique and the results achieved are summarized in the conclusions together with outlook of next steps and future work.

2. Instrumentation, pixel detector Timepix, per-pixel response

2.1. The hybrid semiconductor detector Timepix

The pixel detector Timepix [1] consists of a radiation sensitive semiconductor sensor bump bonded to a pixelated ASIC readout chip (see Fig. 2a, b). The hybrid architecture of the chip-sensor assembly enables to use sensors of different material (Si, CdTe, GaAs) and thickness (e.g., 300, 500, 1000 μm thick). The detector provides a high granularity matrix of 256 × 256 energy-sensitive pixels (total of 65.536 pixels) of pixel pitch 55 um for a total sensitive area 14.08 mm × 14.08 mm = 1.98 cm^2 (see Fig. 2b).

2.2. Miniaturized radiation camera MiniPix-Timepix

In this work a Timepix detector equipped with a 300 μm silicon sensor was used in the readout electronics architecture MiniPix-Timepix (shown in Fig. 2c) described in Ref. [12]. This compact radiation camera is connected by single USB 2.0 cable for power, control and data readout. Operation and online response are enabled by the integrated software tool Pixet [32,33] on any PC or laptop running in high-level operating system (Win, Linux, MacOS). The radiation camera operates as an online active nuclear emulsion [11,34] with response in wide range of particle fluxes, spectral sensitivity (particle energy loss) and direction (wide field-of-view, no collimators needed) [12].

2.3. Quantum-counting sensitivity, room-temperature operation

The dark-current free operation at the pixel level provides single-quantum noiseless sensitivity (photon counting), per-pixel signal processing, high granularity and high-resolution charged-particle tracking response [4,13,35]. The hybrid architecture and per-pixel signal processing electronics of Timepix [1,4] enable room-temperature operation and noiseless quantum-sensitive detection of single particles [8,11]. This capability allows to perform precise measurements of light and heavy charged particles [4,13,22,36] in wide range in terms of event count rate and per-pixel spectral registration. Essentially, all charged particles reaching the sensor active volume are registered. The detection threshold can be expressed in terms of deposited energy which is about 4 keV at the pixel level. X rays and low-energy gamma rays are also registered, albeit with decreasing detection efficiency above few tens of keV depending on the sensor material (Si, CdTe, GaAs) Z-number and thickness (up to 2 mm).

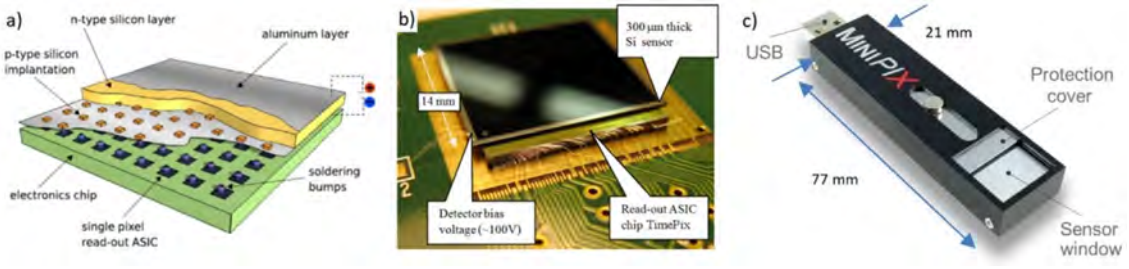

Fig. 2. Illustration (a) and photo (b) of the Timepix chip-sensor assembly. The semiconductor radiation-sensitive sensor (a 300 µm thick silicon sensor was used, illustrated in (a) in yellow) has size 14 mm × 14 mm is bump-bonded to the ASIC Timepix readout chip. The detector provides an array of 256 × 256 pixels (total 65536 independent channels). The miniaturized radiation camera miniPIX Timepix (c) has dimensions 77 mm × 21 mm × 10 mm connects directly to PC or laptop via USB port. (For interpretation of the references to colour in this figure legend, the reader is referred to the web version of this article.)

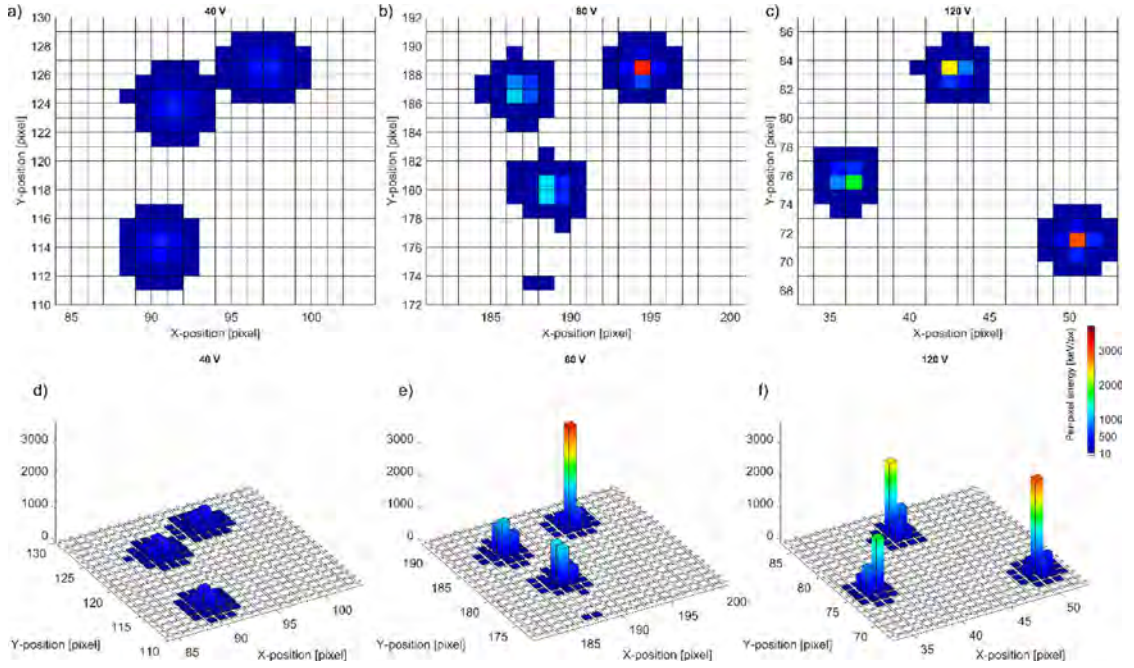

Fig. 3. Detection and spectral registration of alpha particles from an 241 Am source by a MiniPIX-Timepix detector equipped with a 300 µm silicon sensor. Measurement performed in air, at distance 23 mm. Data shown for different sensor bias (three values are shown – 40, 80, 120 V – in columns from left). Single particles are registered as pixel clusters which can be displayed in planar view over the sensor plane (top row) and vertical view (bottom row). The per-pixel energy registration in [keV/px] is displayed in colour and, in the bottom figures, along the vertical axis. The standard low-energy calibration was applied.

2.4. Pixel clusters, charge sharing

Single particles are registered in the pixel detector operating at room temperature in the form of a cluster of adjacent pixels [8,13,22]. Examples are given in Fig. 3. Even when the particle interacts in a few pixels or just in a single pixel, the deposited energy is distributed over many pixels forming a cluster. This is due to charge sharing effect and lateral charge spread in the charge collection process in the semiconductor sensor [37,38]. The extent of this effect is determined by the amount of deposited charge and the charge collection time which is determined by the applied sensor bias and the charge collection distance to the pixelated matrix electrode [8,13]. The registered clusters thus exhibit a spatial broadening with varying distribution of energy registration per-pixel. The charge deposited on the sensor top side, such as that produced by low-energy alpha particles — see Section 3.1, undergo a lateral spread into the adjacent pixels. The extent of this charge sharing effect is determined by the depth position of the deposited charge in the sensor and the applied bias voltage [38,39].

2.5. Spectrometry per-pixel

The Timepix ASIC provides highly integrated signal electronics per-pixel (amplifier, amplitude discriminators, digital counter) [1]. Timepix features a 14-bit ADC and a counter providing a multi-channel analyzer (MCA) of 11.8 k channels per pixel. The MCA can be used to register per-pixel: the number of counted events, the energy, or the time of interaction. Timepix uses a high frequency clock with frequency up to 80 MHz as time/clock reference for per pixel energy or per-pixel time measurements. Each pixel of the Timepix detector can be independently configured to run in one of four different operating modes [1]: (1) Masked mode: pixel is off, (2) Counting mode: 1-count for each signal over threshold (the counter is incremented by one when the energy of the interacting particle crosses the preset threshold level), (3) Time over-Threshold (ToT) or energy mode: the counter is incremented continuously as long as the signal is above threshold (the counter is used as Wilkinson type ADC allowing direct energy measurement in each pixel), and (4) Time-of-arrival (ToA) or time mode: the counter is incremented continuously from the time the first hit arrives until the closure of the shutter (end of the time window or frame acquisition time).

2.6. Per-pixel spectral threshold, resolution and range

The per-pixel detection threshold is low enough to enable the detection of single particles including low-energy X rays and low-LET particles and minimum-ionizing particles such as relativistic electrons and secondary cosmic ray muons [11,13]. For a Timepix chip with a silicon sensor the detection per-pixel threshold is 4 keV. The energy resolution is at the range 5%–8% [26]. The upper range is determined by the proportionality and linearity of the per-pixel preamplifier and further DAC pixel electronics settings such as the discharging time Ikrum parameter. In addition, the applied sensor bias, which determines the extent of charge sharing in the semiconductor sensor operating in room temperature, also influences the extent of charge deposited in the given pixel.

The range and spectral response of Timepix at the pixel-level [29] is illustrated and extended in Fig. 1. The low-energy region ([26] – green) is extended by the high-energy calibration ([27,28,30,31] also this work – blue) and the very high-energy calibration ([29,30] – purple).

The plot shows the relation and dependence of the derived per-pixel energy to the registered pixel time-over-threshold signal. The operational range starts from the per-pixel threshold (e.g., 4 keV for a Timepix chip assembly with a 300 μm silicon sensor) up to nearly 2 MeV with proportional and monotonic dependence. In this proportional range two broad regions are identified [29]. A low-energy region, consisting of a non-linear segment and a linear segment, which is the well-established regular region using a standard calibration [26] – see below. And a high-energy region of partly distorted response consisting of a linear region and a parabolic region. This region is the subject of this work. Above this level, a marked distortion and saturation of the per-pixel spectral response occurs which results in loss of proportionality and unambiguity. This very high-energy region exhibits two distinct segments which have been also identified [29]. The physical reason why distortion at high-energy regions appears is the nonlinear behaviour of charge sensitive preamplifier. It was described in [40] where a single pixel of Timepix sensor was connected to the oscilloscope. The output of preamplifier and output of comparator were probed as a response to high charge inputs. It was shown that for large, collected charges the output of preamplifier saturates and then it undershoots. As the voltage level goes back to zero from the undershoot it triggers the comparator one more time which creates additional false pulse. This false pulse is added to the original one and that causes the nonlinear response of the pixels when large charge is collected.

In our method and selected approach, focused on the high-energy region, we examine and extend the upper operational range of proportionality with unambiguous dependence as described in this work.

2.6.1. Low-energy region: regular dependence

The low-energy region (segments A + B) is standardly calibrated with monoenergetic low-energy gamma rays and characteristic XRF radiation. Three energies are used [26] which are obtained from standardly available radionuclide lab sources ^{241}Am (59.5 keV), ^{55}Fe (5.9 keV) and a XRF line e.g., 24.2 keV from indium or 25.3 keV from antimony coupled to a bench-top X ray unit. Three energies are used to calibrate namely the non-linear part (segment A) and lower-part of the linear segment B. The remaining range (segment B until about 850 keV) is extrapolated.

2.6.2. High-energy region: distorted region

The high-energy region has been examined [41] and calibrated to limited extent with 5 MeV and 8 MeV protons [29,30]. The radiation and energy were chosen to selectively deposit relatively large amount of charge at the pixel level. The incident direction was also exploited to control and adjust the distribution of deposited energy along the particle track. This approach requires a particle accelerator and precise positioning geometry of the detector relative to the particle beam. This region can be also examined and per-pixel energy calibrated with mono-energetic alpha particles from standard radionuclide lab sources such as ^{241}Am. This is the subject of this work. Data are collected in air in a simple setup geometry. Parameters are source-to-detector distance (few positions are measured) and also the detector sensor applied bias voltage — which controls and determines the extent of charge sharing and thus the fractional amount of energy registered by the adjacent pixels in the given cluster. Measurements and sufficient data can be taken within one day, making this technique convenient for simplicity and wide-spread application.

2.6.3. Very high-energy region: saturated region, volcano effect

The very high-energy region has been investigated [41] and partly calibrated using high-LET particles with 8 MeV protons and light ions (40 MeV ^{12}C ions) [29,30]. Radiation sources for calibration of Timepix in this region require a particle accelerator beam. This region no longer exhibits proportionality and loss of signal unambiguity. The pixel response undergoes a marked saturation in the form of reversed proportionality. The resulting volcano effect [41,42] can yield (i) a large deviation of anomalous small values of per-pixel energy [43] (illustrated in Fig. 1) or (ii) a limited deviation of a saturated flat plateau [44]. The first scenario occurs for n-type silicon sensors, in which hole collection proceeds to the pixelated matrix. The second case occurs for p-type sensors in which electron collection proceeds to the pixelated matrix.

3. Experimental, measurements, data acquisition

3.1. Spectral detection of alpha particles, sensor bias

The detection of alpha particles from ^{241}Am and the spectral per-pixel response of the detector is shown in Fig. 3. Data were acquired in air with a Timepix detector equipped with a 300 μm silicon sensor. The detector is operated at room temperature and can be set at varying sensor bias. Single particles are registered in the form of a cluster of pixels the size and morphology of which are determined by the trajectory of the particle across the sensor and the extent of the charge sharing effect in the semiconductor sensor (Section 3.2). A minimum bias voltage is required for depletion of the sensor volume to ensure a complete collection of the deposited charge. For the sensor used (300 μm thick silicon) the full depletion volume is provided above +60 V.

3.2. Cluster energy, cluster height, applied bias, charge sharing

The deposited energy by the particle in the sensor is distributed over several pixels in the cluster. The sum of the individual per-pixel energies of all the pixels in the given cluster gives the *cluster energy* (called also cluster volume) [8,41] and corresponds to the particle deposited energy. The pixel with the largest energy in the cluster is called the *cluster height*.

The consequence of the value of the sensor bias voltage applied can be seen in the alpha particle events shown in Fig. 3. Applied low bias reduces the sensitive depleted volume of the sensor and enables charge loss processes such as charge recombination. Such effects reduce the amount of collected charge and registered energy. Applied low bias also extends the charge collection time and enhances charge sharing. This results in pixel clusters of greater size and of lower cluster pixel height.

Applied high bias on the contrary suppresses charge sharing. The resulting pixel clusters are smaller (smaller number of pixels) which exhibit larger cluster pixel height. For bias values at and above the level required for complete depleted volume of the semiconductor sensor (at/above 60 V for the 300 μm silicon sensor used) the collected charge and registered energy are complete.

Depending on the exact position of the detected particle in the central hit pixel, the registered cluster pixel height can vary over a range of values. Alpha particles interacting in the middle of the central

pixel deposit a greater amount of charge in the central i.e., cluster height pixel. Conversely, particles interacting in the periphery of the central hit pixel, spread out a greater part of the deposited energy to the adjacent pixels and deposit lower energy in the central hit pixel. This effect can be used to adjust and select the amount of energy collected by the central hit pixel as shown in Sections 4.6 and 4.7.

3.3. Setup, varying deposited energy, varying sensor bias

The task is to provide the selective deposition of well-defined energy at the pixel level in this range. In order to make the method as simple as possible, we use mono-energetic alpha particles from a standard radionuclide source (^{241}Am). Measurements are performed in air in a simple geometry — see Fig. 4. Data are collected for varying alpha particle energy — achieved by setting the source-to-detector distance at various positions. To minimize the spread of the particle energy, we use a laboratory spectrometric ^{241}Am source manufactured with a thin cover layer (< 1 μm) – suitable for spectrometry and precise calibration measurements. The energy of the alpha particles arriving to the detector was varied as well as the extent of per-pixel energy registration. This is described below together with the important effect of source-to-detector distance and the applied sensor bias voltage.

3.4. Source-to-detector distance, variation of the particle deposited energy

The source-to-detector distance was varied over the range of 20–30 mm in steps of about 1 mm. This allows to have particles of varying energy within a certain range in order to change and tune the alpha particle energy. The particle deposited energy and in particular the per-pixel energy, which is critical especially for the central pixels and cluster height, are selectively registered. The aim is to collect clusters having per-pixel energy and cluster height range within the well-established low-energy calibration [26]. This limited per-pixel energy range goes up to about 850 keV for Timepix with a 300 μm thick silicon sensor. The remaining collected clusters, those having per-pixel energy and cluster height above this level, also serve and will be used in a latter step of the high-energy calibration procedure.

3.5. Applied sensor bias, variation of charge sharing extent

The detector sensor bias voltage was also varied (values examined over the whole bias range from 0 V thru +200 V for the 300 μm Si sensor). The applied bias creates the depleted volume and also affects the extent of the charge sharing [8,38]. Spectrometric measurements were examined and performed with applied bias in wide range. At high bias the charge sharing is suppressed and the extent of radial spread is limited. At low bias the charge spread is enhanced and thus the deposited charged is distributed among many adjacent pixels [8,41]. The amount and extent of deposited and collected charge in the pixels in the cluster can thus be varied and adjusted. This tool is especially sensitive for the central pixels with the largest per-pixel energy registration.

3.6. Data acquisition

The per-pixel energy registration was examined in extended range in terms of deposited energy and per-pixel energy by combining and jointly varying the source-to-detector distance and the applied sensor bias voltage. Systematic irradiation measurements were performed with bias voltage from +70 V up to the maximum +200 V. Data were collected in applied bias steps of 10 V and for several distances in the range of 20–30 mm. Given the geometry and setup used, the energy of the alpha particles reaching the detector acquire a spatial spread over the detector pixel matrix (see Section 4.4). This is due to the close geometry (small source-to-detector distance) which results in different paths travelled by the particles according to the position on the detector. The particles travel different distance trajectories in air and across the detector non-sensitive thin layer and also across the source thin coating cover.

To collect enough statistics an average of few tens of events were collected for each pixel for each setting. An event is understood as a pixelated cluster reaching each given pixel. The activity of the ^{241}Am source was 11.98 kBq. Data were collected on average at a rate of or around 300 clusters per second. The detector frame acquisition time was in the range 10–100 ms in order to register only isolated events without event pile-up. At this rate the collection of all data was done within 24 h. Measurements are performed in air.

4. Per-pixel high-energy calibration, alpha particle spectrometry

4.1. Deposited energy registration, applied sensor bias

The registered deposited energy of mono-energetic alpha particles from a ^{241}Am source by Timepix as a function of bias voltage applied on the detector sensor is shown in Fig. 5a. Data shown were collected in narrow bias steps over the range of 0–200 V for one sensor-to-detector position (15 mm distance) which provides one alpha particle energy (about 3.5 MeV at the detector central position — closest position perpendicular to the source). Due to the relatively close source-to-detector distance, there is a spread (reduction) in the energy of the alpha particles arriving to the periphery regions in the detector. The registration of deposited energy is distorted namely for low bias values by incomplete sensitive volume depletion of the semiconductor sensor. The nominal bias range between 42 to 70 V is constant (fixes at 42 V) due to voltage source range malfunction in the embedded voltage source component used in the MiniPIX-Timepix electronics board. Above this level the whole deposited charge is collected. At high bias values above 70 V an increase in the registered energy is noted which is due to the saturation of the per-pixel spectral response namely in the cluster central pixels which collect the largest charge. In the plot the most probable values are given for data collected at each bias value measured (see below). The difference with the expected value is due to distortion of the per-pixel energy response for high-energy deposition (subject of this work) and uncertainty in the extrapolation of the low-energy calibration [26] to high-energy region.

4.2. Alpha particle deposited energy spectrum, cluster volume

The resulting deposited energy spectrum is given in Fig. 5b. Data are shown for four selected values of the sensor bias. The data vary according to the sensor bias value. At low sensor bias, below the depleted volume level, the deposited energy is only partly registered. There is an underestimation in the registered deposited energy. At medium-range values of sensor bias, such as 71 V, the extent of charge collection increases, reaching the full depleted volume providing a proper and complete collection of deposited charge. The spectrum shifts towards higher energy. At high sensor bias values, i.e., > 71 V for the 300 μm silicon sensor used, the deposited charge is fully collected. However, the registration of per-pixel energy becomes distorted due to change in the proportionality of the per-pixel spectral response. At high sensor bias values, this anomalous effect is amplified especially for the cluster central pixels which collect the large part of the deposited energy. Also, part of the spectrum significantly departs from the main component — note the new high-energy component in the high bias data spectrum. This corresponds to clusters with large per-pixel energy deposition, for which the spectral distortion is the greatest. The resulting registered values, if uncorrected, yield overestimated values larger by up to a factor of two and more.

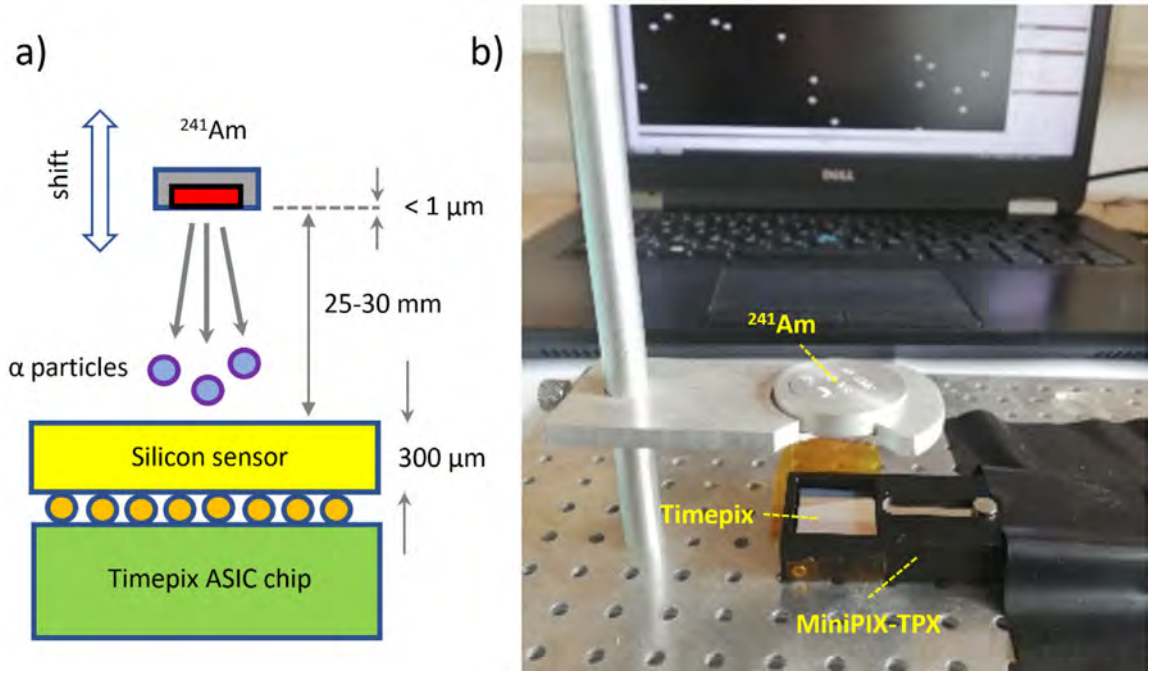

Fig. 4. Illustration (left) and photo (right) of the experimental setup. Measurements are performed in air. The energy of the alpha particles is tuned by shifting the source-to-detector distance (values used between 25–30 mm in steps of about 1 mm). The Timepix detector was equipped with a 300 µm silicon sensor operated in the MiniPIX-Timepix.

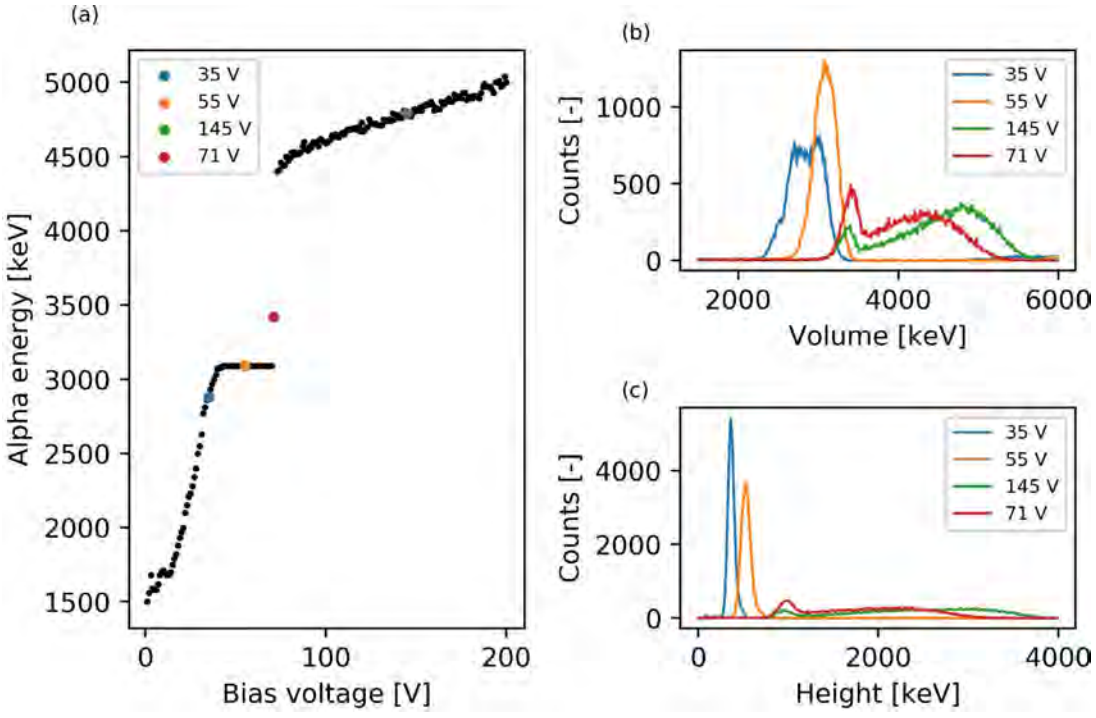

Fig. 5. Spectrometry of alpha particles from ^{241}Am source with a MiniPIX-Timepix detector equipped with a 300 µm Si sensor. Results shown for different bias sensor voltages. Data were collected in air and are shown for one sensor-to-detector position (23 mm distance). The corresponding alpha particle energy was centred at about 2.6 MeV. (a) Measured deposited energy (spectra maxima) according applied sensor voltage (range from 0 to 150 V in steps of 2 V). In the range 42 to 71 V the sensor bias value supplied by the detector voltage source sensor is constant (fixed value 42 V). Selected bias values, 35, 55 (i.e. 42), 71 and 100 V — highlighted in colour in (a), are processed for (b) deposited energy spectra (cluster volume) and (c) distribution of the highest per-pixel energy value (cluster height). Energy values are derived using the existing low-energy per-pixel calibration [26].

4.3. Per-pixel energy response, cluster pixel height

In order to examine this effect, the per-pixel energy registration is analysed. The distribution spectrum of the energy registered by the pixel with the largest value in the given cluster or cluster height, is shown in Fig. 5c. The central pixel in the cluster registers the largest energy for the type and energy of the radiation used (few MeV alpha particles). The range of such particles in silicon is few tens of µm, well within one pixel. These settings allow to selectively deposit a well-defined amount of energy in a small volume in the detector, namely

within one pixel. The fraction of the total charge deposited in the central pixel is determined by the extent of charge sharing and can be modified by the applied sensor bias [41]. This can be observed in the cluster height spectrum (Fig. 5c). For high sensor bias, such as 100 V, the distortion increases, and a significant component acquires too large values well above the 850 keV level between the regular low-energy region and the distorted high-energy region. These large height events produce the broad high-energy component in the height spectrum at high sensor bias and correspond to clusters for which a large portion of the energy deposited by the alpha particle was collected by the central pixel. The position of interaction for these events occurs well within the central pixel, far from neighbouring pixels. On the other hand, the narrow low-energy component in the height spectrum, corresponds to events in which the position of interaction of the alpha particle was in the vicinity of two or also three and four pixels. For such events, the large central part of the deposited charge is more evenly distributed among two and more pixels, and thus the cluster height values become smaller. For these, the per-pixel distortion at large per-pixel energy is limited.

4.4. Spatial spread and broadening of the deposited energy

The setup and geometry used were designed for maximum simplicity. The energy of the mono-energetic alpha particles arriving to the detector spreads over the pixel matrix position. This is due to the varying trajectory of the particle between the source and the detector sensor. Part of the trajectory goes across the protective seal of the ^{241}Am source (thin metallic/Al coating < 1 μm) and across the common electrode layer of the pixel detector (also thin metallic/Al coating $<$ 1 μm). Moving away from the perpendicular direction towards non-perpendicular direction, the path length across these layers varies thus it reduces and broadens the particle energy (see Section 3.4). In addition, the trajectory across few cm of air reduces the particle energy and broadens the resolution. The broadening takes the form of spatial spread in the radial direction perpendicular to the source-to-detector axis. For a given setup, i.e., fixed source-to-detector distance, the extent of energy spread is up to 5%.

4.5. Data processing

Data for different bias voltages and various source-to-detector distances are processed, arranged and analysed for each pixel separately. This follows the data pre-processing of the raw signals by single particles in the form of pixel clusters registered event-by-event. Morphology and spectral cluster analysis parameters are derived such as volume (particle deposited energy), cluster size (number of pixels in cluster), cluster height (energy of the pixel with largest energy, denoted in this work also as the brightest pixel). In addition, the height of the second brightest pixel is saved separately for each pixel with calibration coefficients of per-pixel calibration. Information about cluster size can be used for an additional filtration of data. That helps to reduce the amount of data and improve the processing speed.

4.6. Reference alpha particle energy, cluster height cut-off, event filtering I

A key step in the high-energy per-pixel calibration is to determine the reference energy of the alpha particles. The reference energy is given by the specific source-to-detector distance and also by the radial position of the event hit over the detector pixel matrix. Due to relatively close geometry, the energy of alpha particles arriving to the detector acquires a lateral spread. This is due to the particles traversing a different distance in the air and across the thin non-sensitive electrode layer on the top of the sensor surface.

Events for calibration are filtered in such a way that only clusters with cluster height values of limited range are selected. A maximum cluster height cut-off is set 850 keV. This level is within the upper range of extrapolation for the existing low-energy calibration. The selected limited-height cluster events are processed with the low-energy calibration. Fig. 6 shows the distribution of cluster volume (i.e., particle deposited energy) and cluster height for the filtered events (i.e., with cluster height values below the filter cutoff 850 keV) for one pixel. The cluster volumes of the filtered data are z-scored. Data exceeding one sigma are labelled as outliers. One sigma data points are averaged, and the mean value is used as a reference alpha energy (red dash line). The reference alpha energy is calculated for each pixel and each distance.

The derived reference alpha particle energies spreads over a range of values over the pixels in the detector. The corresponding spatial distribution across the detector pixel matrix is shown in Fig. 7. The plots correspond to one measuring setting (one source-to-detector distance) and over several sensor bias voltages. The derived distribution matrix (Fig. 7a) is filtered by median convolution filter (Fig. 7b) to remove artifacts that are caused by uneven distribution of alpha particles over the pixels. Some pixels have zero hits. The low-pass Gaussian filter (Fig. 7c) is used to remove high frequencies and to smooth the matrix. The resulting matrix distributions provide the necessary reference energy for all pixels.

4.7. Events above cluster height cut-off, event filtering II

Cluster events with heights above 850 keV are used in a second step. The basis of the high-energy calibration is to relate and evaluate the clusters with only one pixel that exceeds the per-pixel cluster height cut-off (exceeding pixel) to the reference cluster energy. Hence, the energy of the exceeding pixel equals to the difference between the reference energy and the energy of a cluster excluding the hot pixel. This method was used in previous work [29,45]. Clusters with two or more exceeding pixels are filtered out so only clusters with one exceeding pixel are processed. For that reason, the energy of the second brightest pixel is saved along with volume and height. The resulting cluster height energy in [keV] can be plotted as a function of uncalibrated cluster height in [ToT] as shown in Fig. 8.

4.8. Exceeding pixel calibration, distinct regions, data fitting

As can be seen in Fig. 8, the derived high-energy range per-pixel energies deviate from the extrapolation of the low-energy per-pixel calibration. The data points exhibit moreover different dependence in two regions: (i) One region (labelled C) from approximately 800 keV to 1000 keV showing a linear dependence that only partly departs (small decrease) in slope from the extrapolated low-energy per-pixel calibration, (ii) a second region (labelled D) above about 1000 keV which exhibits a marked increase partially non-linear.

The per-pixel spectral response is fitted in both regions. For fitting the functions, the X axis and Y axis are swapped and then both regions are separated by kernel density estimator (KDE). The KDE can estimate the probability density function of data point in ToT pixel volume axis. This function has a sharp peak in the linear region and quickly falls close to zero. For separation of the two regions the first differentiation of KDE is used. The separation point is defined as the first positive value of KDE differentiation after its minimum. Data points that lie below the threshold are fitted with a straight-line function Eq. (1). Data points above the threshold are fitted with a parabolic function Eq. (2).

$$Y = A_2 X + B_2 \tag{1}$$

$$X = A_3 Y^2 + B_3 Y + C_3 \tag{2}$$

The X is pixel deposited energy in terms of keV and Y is pixel deposited energy in terms of ToT. After the least square fitting the residuals are calculated and data points with residuals larger than 1.5 sigma (exclusion threshold) from mean are discarded as outliers. The rest of the points are least square fitted again. The data fitting process is summarized and depicted in Fig. 9. It can be seen that the datapoints

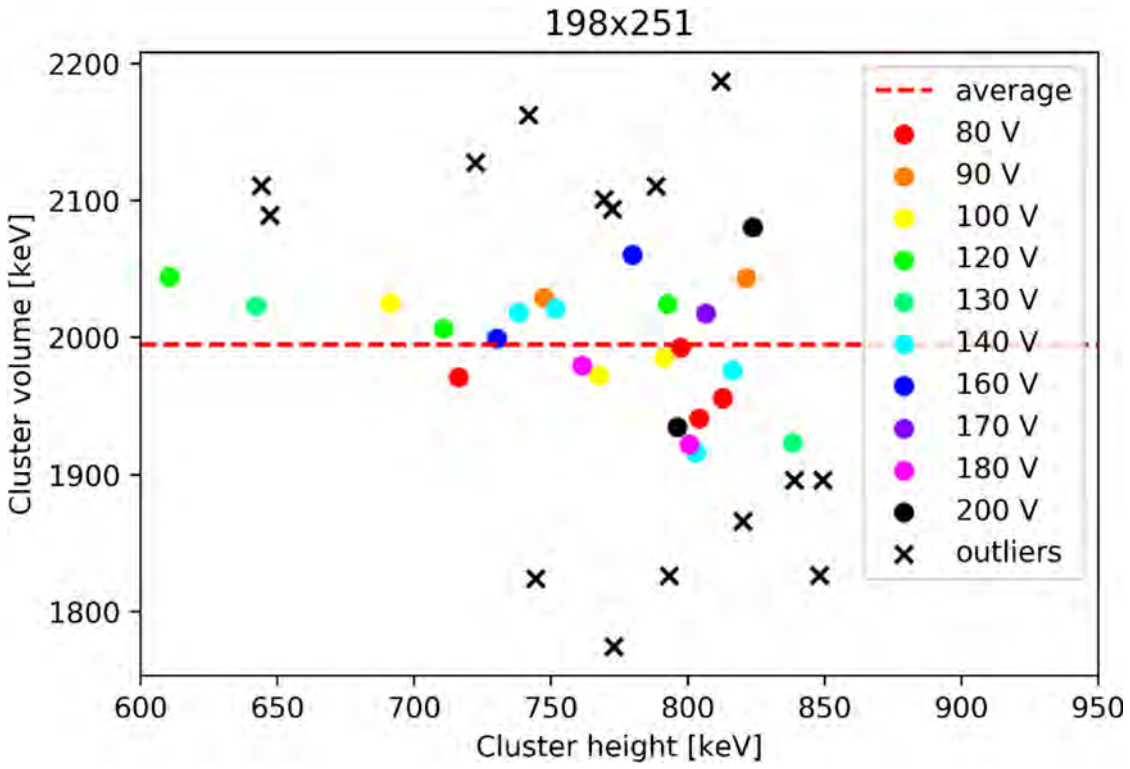

Fig. 6. Plot of alpha particle deposited energy (Y axis) versus cluster height (X axis) for one measuring setup (fixed source-to-detector distance 28 mm) and varying sensor bias values (see colour inset). Data shown for one pixel (pixel coordinates 198 × 251). Energy data values derived using the existing low-energy per-pixel calibration [26]. (For interpretation of the references to colour in this figure legend, the reader is referred to the web version of this article.)

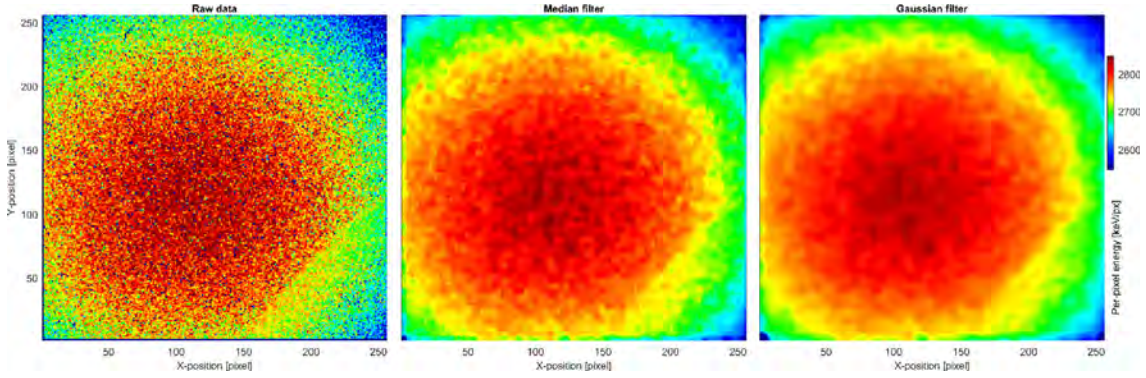

Fig. 7. Distribution of deposited energy by filtered alpha particles over the detector pixel matrix: The raw distribution (left) is processed with Median filter (middle) and Gaussian filter (right). Data shown for one source-to-detector distance (20 mm) over the wide range of bias values (70–150 V).

have large spread. This spread is caused by the averaging of reference energy. Hence the less frequent depositions of energy for example from an extreme angle will be compared with the reference energy that was calculated as the mean of many datapoints. Such comparisons will cause the observed large spread. The discarding of events which are not within exclusion threshold can be rationalized as an attempt to exclude clusters that arrive from extreme high or low angles and clusters that lost unusually large or small portion of energy due to energy straggling (in the source and in the air). This processing step can be understood as a physical collimator that accepts only particles coming from certain angle.

The residual plots can be used to evaluate the goodness of fit. The residuals are defined as difference between the theoretical values of the fit and the real measured values. In our case the residual values are directly influenced by the exclusion threshold. The lower the exclusion threshold the higher the spread of residuals and vice versa. The discarding of outliers artificially forces the datapoints to shape as the fitted function which enhances the determination coefficient and lowers the residuals. Therefore, to assess the goodness of fits the residual plots of original unfiltered data of one random pixel are shown in Fig. 10. In general, the precise models should have randomly scattered residuals around zero. In the most part of the fit the residuals are randomly scattered around zero. The problematic part of the fit is the transition between linear and parabolic fit which shows a pattern behaviour. Therefore, it can be assumed that the chosen model has certain shortcomings especially in the transition region. On the other hand, the proposed model is relatively simple, robust and can be easily applied. We have decided to use the proposed model as a compromise between the simplicity, robustness, and its correctness.

4.9. Regions of different proportionality, fitting functions

The per-pixel energy calibration exhibits regions of distinct response of different proportionality. The response in wide energy range for one

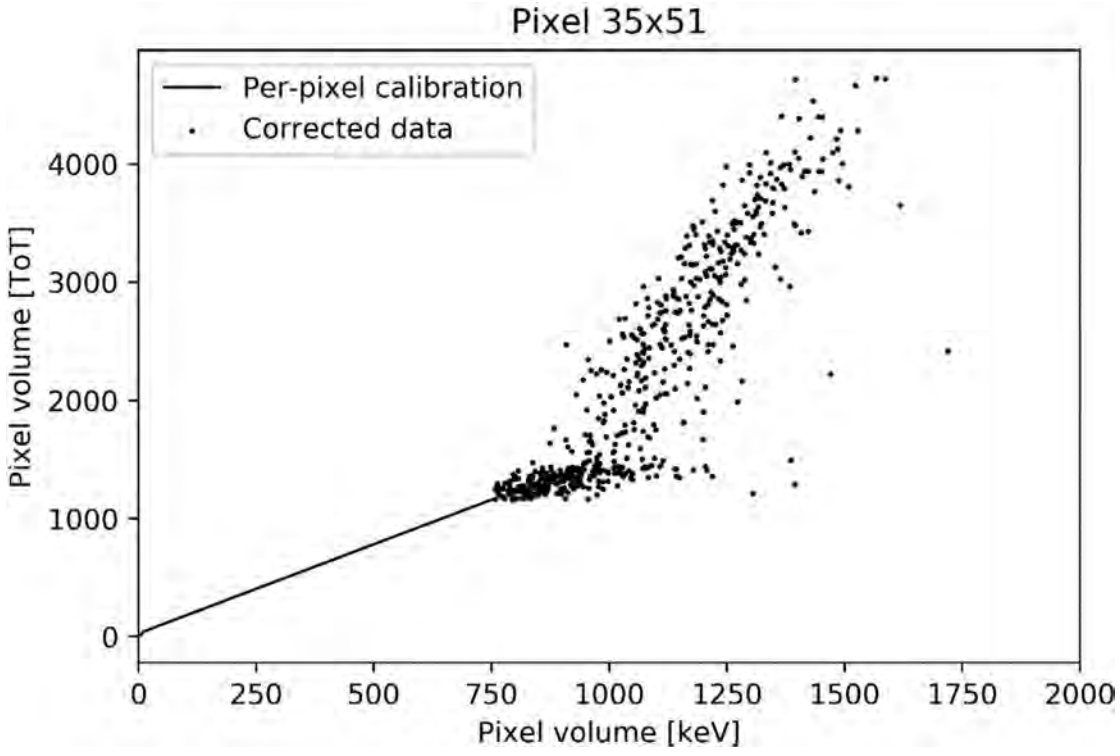

Fig. 8. Per-pixel high-energy response derived with the developed high-energy calibration. The uncalibrated raw data given in [ToT] is plotted on the Y axis. The derived calibrated per-pixel energy given in [keV] is plotted on the X axis. Data shown for one pixel (coordinates 35 × 51 in the pixel matrix). The low-energy region with the existing low-energy calibration is included.

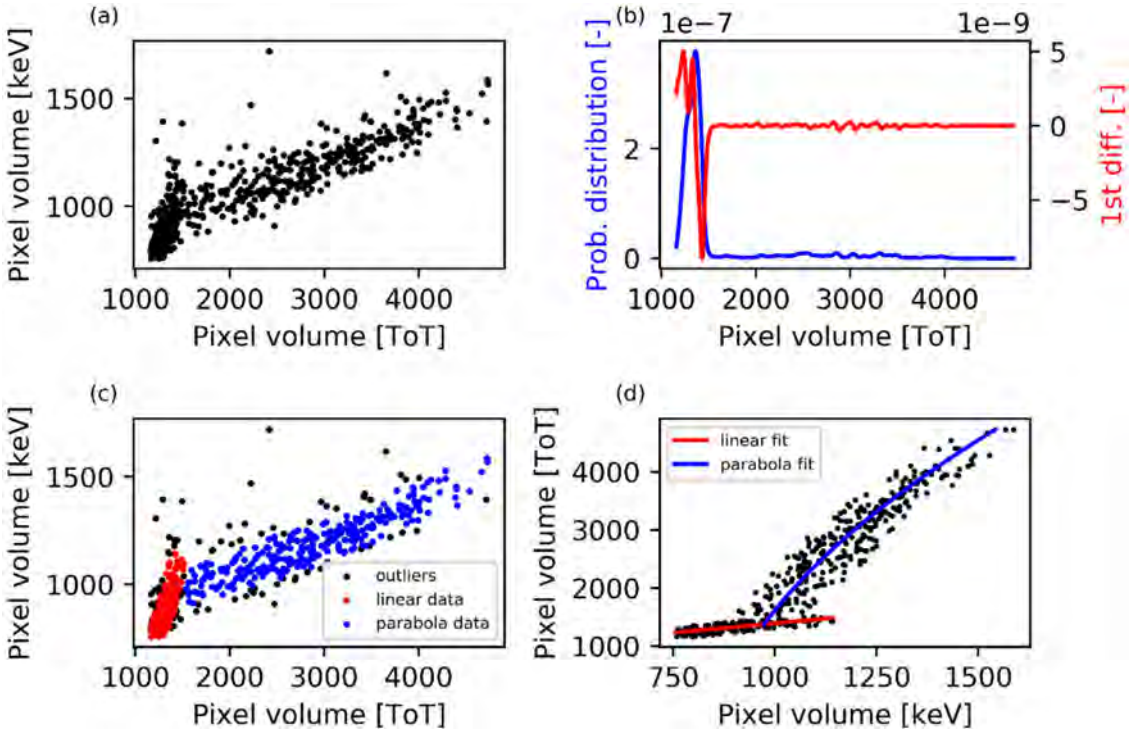

Fig. 9. High-energy calibration datapoints processing steps. Data and figures shown for one pixel. Firstly, (a) the axes are swapped in Fig. 8. Then, (b) the Kernel Density Estimation (KDE) of the datapoints (blue curve) and its differential (red curve) are calculated. The transition point is determined as the position where the differential (Y-axis scale on right) reaches positive values going from negative. The datapoints in the two regions are fitted by a line and a parabola function. Datapoints that are not within 1.5 sigma from the fitted functions are removed and the functions are recalculated (c). The axes are swapped back (d) and the transition point T3 is calculated as the intersect of the linear and parabolic functions. (For interpretation of the references to colour in this figure legend, the reader is referred to the web version of this article.)

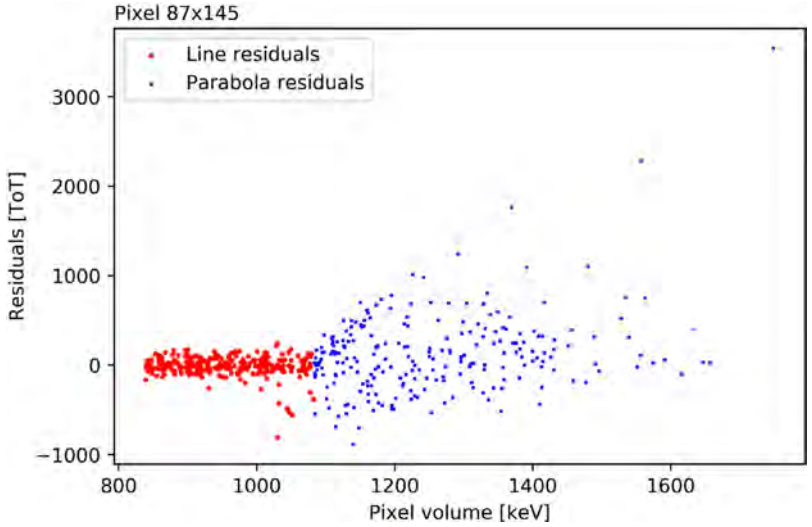

Fig. 10. Residual plot of one random pixel. Residuals show the difference between linear and parabolic fit and datapoints.

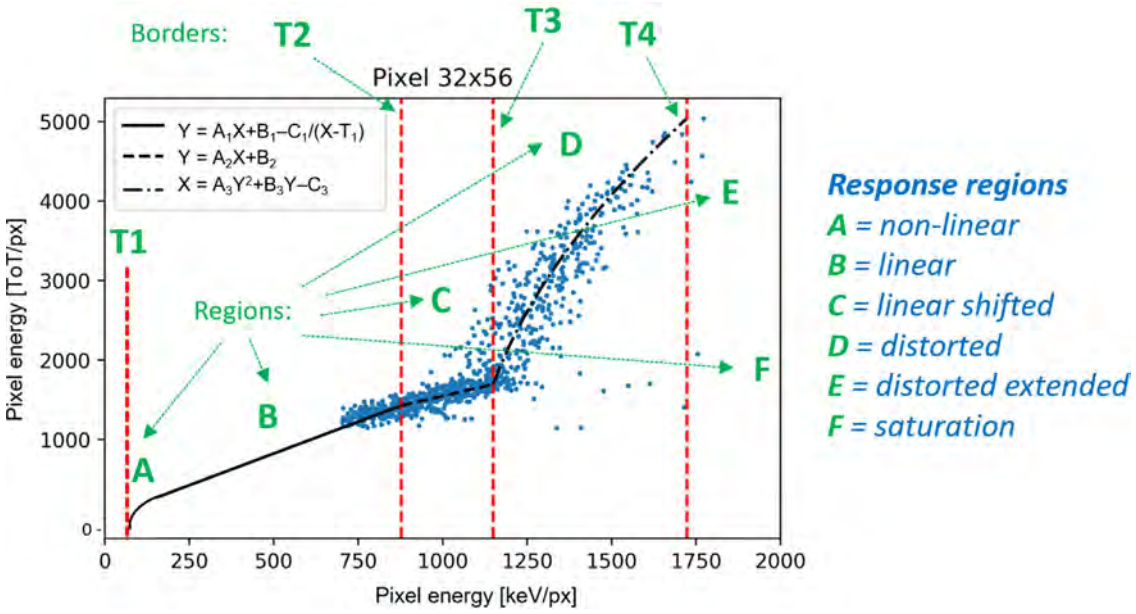

Fig. 11. Pixel energy calibration in wide-range consisting of the existing low-energy region (A+B), the newly described high-energy region (C+D), and the distorted and saturated region (E+F). Data shown for one pixel (pixel ID coordinate given on plot heading) collected over various bias values and source-to-sensor distances. The calibration exhibits distinct regions of per-pixel spectral response (labelled A thru F, listed on right) which are separated by threshold levels (T1 thru T4). The regions of monotonous proportionality (A, B, C, D) are described by parametric fitting functions.

pixel is shown in Fig. 11. Data are shown for one pixel collected over various source-to-detector distances and sensor bias values. The figure includes labels and marks for distinct regions of proportionality.

The regions of monotonic proportionality consist of the existing low-energy region which is labelled A and B, denoting the non-linear and linear segments, and the newly described high-energy region C and D, corresponding to regions of different dependence. The region thresholds T1 thru T4 determine the borders between region function dependence. T1 corresponds to the low-energy per-pixel detection sensitivity threshold. The derivation of the upper threshold provides the maximum applicability of the high-energy per-pixel calibration method presented and is determined as the maximum of the uncalibrated data point ToT used in the parabolic fit in region D.

4.10. Fitting coefficients of the calibration functions

The fitted calibration functions for the per-pixel energy response describe the well-defined regions A+B, C, and D which exhibit monotonous proportionality. The functions and parameters are listed in Fig. 11 (see inset). The parameters are described in Table 1.

The distribution of values of the fitting calibration coefficients over the detector pixel matrix are given in Figs. 12–15. The corresponding value histograms are included (bottom figures). Fig. 12 shows the A1, B1, C1 coefficients from the low-energy region A+B. Fig. 13 shows the A2, B2 coefficients of the high-energy region, the linear segment C. The threshold upper border T4 of region D is included. The T4 coefficient is calculated as the energy of last fitted datapoint. Fig. 14 shows the coefficients A3, B3, C3 of the quadratic fit of the high-energy region D. Fig. 15 shows the transition threshold borders T1, T2, T3. The

Table 1
Calibration coefficients for the fitting functions (listed in inset in Fig. 10). See text.

Parameter	Description	Region, [border]
A_1, B_1, C_1, T_1	Low-energy region calibration coefficients	A+B
A_2	Slope of line in region C	C
B_2	Y-intercept of line in region C	C
A_3	Quadratic component of parabola in region D	D
B_3	Linear component of parabola in region D	D
C_3	Constant component of parabola in region D	D
T_2	Threshold border between B and C regions	[BC]
T_3	Threshold border between C and D regions	[CD]
T_4	Upper limit of high-energy range per-pixel calibration	[D]

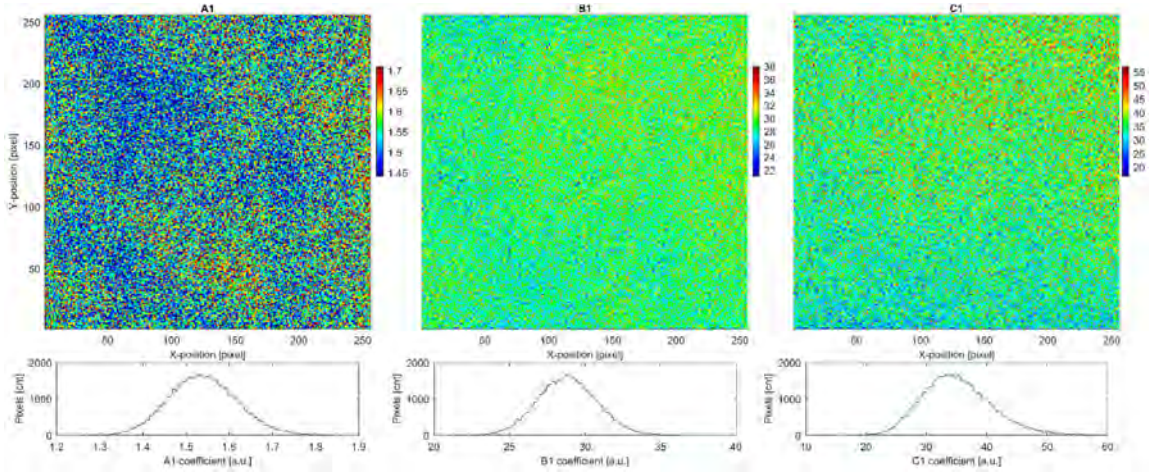

Fig. 12. Fitting calibration coefficients A_1 (left), B_1 (middle) and C_1 (right) displayed as spatial distributions over the detector pixel matrix (top) and histogram distributions (bottom).

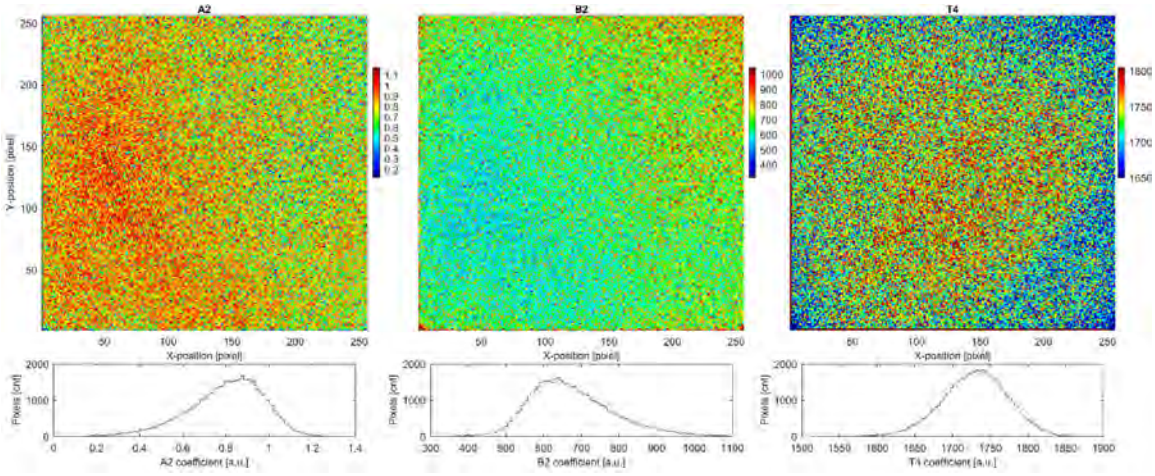

Fig. 13. Fitting calibration coefficients A_2 (left), B_2 (middle) and T_4 (right) displayed as spatial distributions over the detector pixel matrix (top) and histogram distributions (bottom).

coefficient T2 is calculated as the intercept of low-energy calibration line and line in region C, coefficient T3 is the intercept of region C line and region D parabola.

The coefficient A_2 determines the slope of calibration line in region C. The coefficient A_2 is significantly lower than the slope of low-energy calibration function determined by the coefficient A_1 (medians of A_1 and A_2 are 1.55 and 0.85 ToT/keV, respectively). Therefore, the measured energy of particles with cluster pixel heights in this region will be underestimated if only the low-energy calibration is used. The coefficient T2 which determines the transition border between regions B and C has a relatively narrow distribution with median around 840 keV and most of the pixels are distributed in a range of 800–900 keV.

The coefficient A3 of the quadratic function determines the curviness of the function in the region D. The spread of A_3 is relatively large which causes some pixels to have almost linear dependence. Many pixels are curvier, and their steepness slowly decreases. For the most part of the D region, the high-energy calibration function "lags" behind the low-energy calibration curve. Therefore, clusters with heights in region D will be most likely overestimated compared to the real deposited energies. The coefficient T3 that identifies the transition border between shifted linear region C and distorted region D has a much broader spectrum than T2. It spreads in the range of 850–1300 keV causing a large spread of length of shifted linear region C. For some pixels the region C is only several tens of keV wide while for others it spreads over few hundreds of keV. The coefficient T4 which

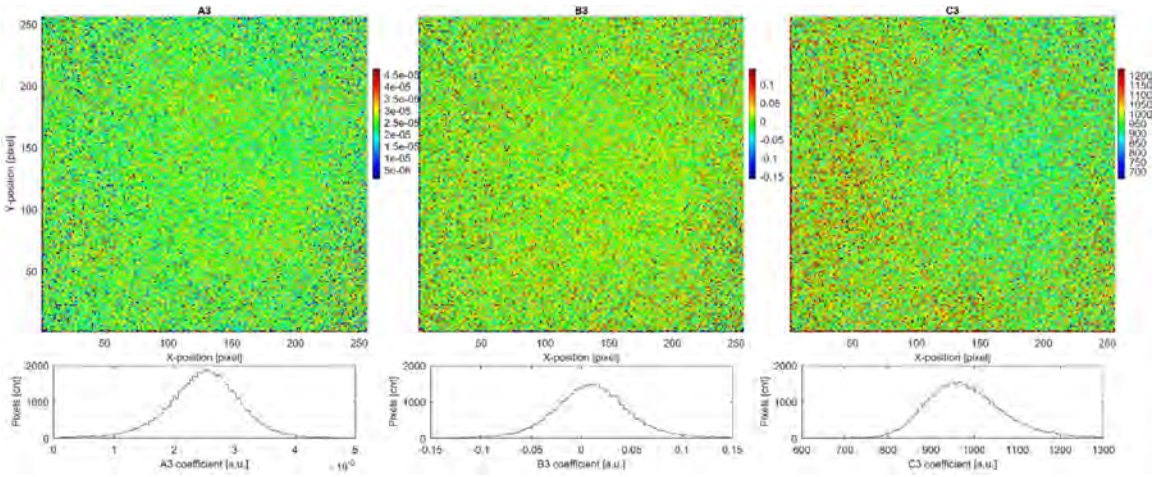

Fig. 14. Fitting calibration coefficients A_3 (left), B_3 (middle) and C_3 (right) displayed as spatial distributions over the detector pixel matrix (top) and histogram distributions (bottom).

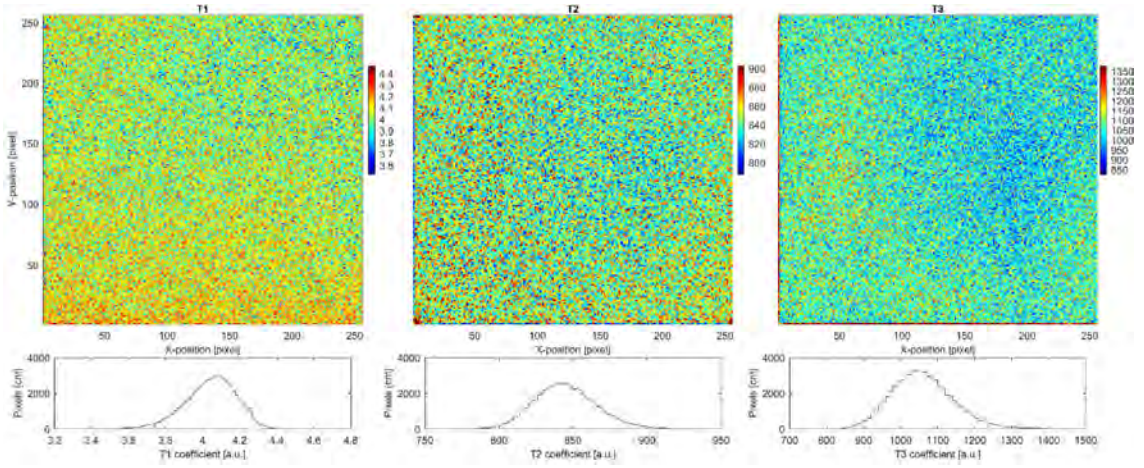

Fig. 15. Fitting calibration coefficients T_1 (left), T_2 (middle) and T_3 (right) displayed as spatial distributions over the detector pixel matrix (top) and histogram distributions (bottom).

Table 2
Pearson cross-correlation coefficients among the calibrating coefficients. See text.

	a1	b1	c1	t1	t2	a2	b2	t3	a3	b3	c3	t4
a1												
b1	-0.324707											
c1	-0.197138	0.363647										
t1	0.179643	-0.098267	-0.959689									
t2	-0.067150	0.209054	0.192504	-0.145363								
a2	0.621926	-0.351145	-0.214073	0.160893	0.126384							
b2	-0.272977	0.328585	0.209558	-0.137997	-0.108728	-0.915079						
t3	0.719868	-0.458500	-0.219838	0.141807	0.055372	0.710877	-0.518682					
a3	-0.230366	0.058828	0.022427	-0.021821	0.002905	-0.027221	-0.086446	0.008142				
b3	0.143994	-0.106167	-0.006876	-0.015649	-0.014955	-0.027117	0.105391	-0.093197	-0.963211			
c3	0.346481	-0.206830	-0.136954	0.105724	0.044001	0.454196	-0.387867	0.709359	0.659883	-0.760419		
t4	-0.014579	-0.010386	-0.055557	0.054820	-0.082784	0.041957	-0.080628	0.260752	0.328394	-0.348876	0.424405	

corresponds to the maximum reliable measured energy has a strong imprint of the ^{241}Am source. Most pixels have T4 coefficient between 1650–1800 keV which is at least double of the low-energy calibration range. The disbalance between pixels in the middle and on the edges

of the chip is caused by the geometry of measurement. This effect was diminished by irradiation of the chip from several distances. To even the disbalance even further it would be beneficial to use the ^{241}Am source with active surface of at least the same size as the detector chip or larger. The active surface of the used alpha source was only 6 mm in diameter.

We examined the correlation among the calibration coefficients. The Pearson coefficients determine the linear correlation between two variables. Each coefficient was calculated from 2 × 65536 values. The resulting values are given in Table 2. The Pearson coefficients close to 1 or −1 indicate a strong linear correlation between the variables. Paired calibration coefficients exhibiting large correlation are C1–T1, A2–B2, A3–B3, and significant correlation are A1–T3, A2–T3, C3–T3, A3–C3, A1–A2. The A2 coefficient has a strong negative correlation with B_2, hence the lower the line slope is the larger the y-intercept is. Interestingly, A2 has also relatively strong correlation with A_1 slope thus the slope in linear shifted region can be estimated solely from the knowledge of A_1 coefficients. Moreover, both coefficients A1 and A2 have a positive correlation with T3 which separates shifted linear region C and distorted region D. In other words, the steeper the slope, the higher the threshold T3 is. All coefficients of the quadratic functions exhibit a strong correlation among each other. The constant coefficient C3 is also correlated with T3.

5. Results, deposited energy spectra, cluster pixel energy height distributions

We evaluate and compare the newly developed high-energy calibration by processing the collected data. We separately apply (i) the existing low-energy calibration [26] and (ii) the new high-energy calibration.

5.1. Extrapolated low-energy per-pixel calibration, alpha particles

The evaluated results can be shown first when they are derived using only the low-energy per-pixel calibration [26]. The resulting deposited energy spectra denoted also cluster volume, and the cluster pixel height distribution are given in Fig. 16. In this approach, the low-energy calibration is applied over the entire per-pixel energy range by extended extrapolation of the low-energy calibration region A+B into the high-energy region C+D.

The resulting deposited energy spectra differ from the expected value and show a large discrepancy among data from different sensor bias voltages. The low bias data (40 V) underestimates the expected deposited energy. This is due to loss of charge collection in the partly depleted volume. The high bias data (80, 100, 120 V) on the other hand overestimate the expected deposited energy. This is due to the application only of the low-energy calibration and in particular the large extrapolation of the calibration function from region B to the high-energy region C+D. This effect results from the large overestimation of the pixel energy at values above the cut-off level or BC region threshold border (at around 850 keV). This can amount to up to few MeV per pixel and applies namely for the hit pixel and adjacent central pixels close by to the particle interaction position. Charge sharing determines the extent of this effect. Enhanced charge sharing, provided by low applied bias, suppresses and reduces this effect. Limited charge sharing, provided by high applied bias, amplifies this effect. The extent of charge sharing and application of only the low-energy per-pixel calibration, accounts for the discrepancies in the deposited energy spectra.

The high bias spectra exhibit the main component as two peaks. The narrow peak at lower energy corresponds to clusters with limited pixel height values which fall within or not too far from the low-energy linear cut-off level around 850 keV (Section 4.6). Such events are those when the particle interaction position occurs in or near the border between adjacent pixels. In these cases, the large local deposited energy is distributed evenly among two and more pixels. Such events are those used in the first step of the calibration procedure (Section 4.6). The large broad peak at higher energy corresponds to clusters with large cluster height values well above the cut-off level. These events correspond to clusters with interaction point well inside the central pixel away from borders with the adjacent pixels. These events were used in the second step of the calibration processing procedure (Section 4.7). In addition to the main component in the spectra, produced by single events, there are also multiple events from two and more alpha particles collected and processed as a joint merged event. Such a doublet events can be seen in the deposited energy spectra at low bias (small broad peak at high energy at around 6 MeV) and the gradually increasing broad component for the high bias data above 6 MeV. The position of this doublet component, e.g., at 6 MeV for the low bias data, also indicates a distortion (underestimation) to the expected value (twice the value of the single event main component which for the data setting used in these plots should be centred at around 3.4 MeV).

The cluster pixel energy height distributions exhibit similar patterns which are related to the patterns in the deposited energy spectra. Low bias data exhibit a dominant narrow component of energy within the range of the low-energy calibration. The low value of the height energy of this peak reflects the loss of charge collection occurring in the incomplete depleted volume due to the insufficient bias voltage applied. The high bias data produce higher values and exhibit a spread-out distribution which splits into two components. A lower energy narrow part and a dominant broad high energy part resulting from the effects described above. The resulting values significantly overestimate the expected values. This can be seen in Fig. 11 by visualizing the further extrapolation towards higher energies of the calibration of region B. This approach extends yet more the linear function of region B, which for most of its range is already extrapolated (see Section 5.5), into the high energy regions. Besides the large overestimation this approach also provides an increased uncertainty in the resulting cluster pixel height values.

5.2. High-energy per-pixel calibration, alpha particles

The data are evaluated with the developed high-energy calibration. The resulting deposited energy spectra and cluster pixel height distribution are given in Fig. 17. The data and results shown correspond to the same set of data used in the previous section Section 5.1 where only the low-energy calibration is used on the acquired data. The difference and results achieved by the high-energy calibration arise at the pixel-level and at the whole deposited energy level.

The deposited energy spectra exhibit a clear dominant single-cluster component with maxima more localized and at the correct position. The spectra are better defined i.e., exhibit a narrow distribution width. This is the case for data of different bias values, namely the high bias data which provide a complete depleted sensor volume. These data exhibit peak maxima position of correct value (3.4 MeV for the data setting used in the figure). The low bias data, in which charge collection loss occurs, exhibits an expected position shift to lower energies. In addition to the main single-event peak, a doublet component is registered at higher energies. For the high bias data, it appears at correct position (twice of the single cluster component value at 3.4 MeV) and exhibits a narrow distribution width. The low bias data exhibits a doublet component of lower energy and broader distribution width due to the loss of charge collection in the partially depleted sensor volume.

The cluster height distribution for high bias data exhibits a clear component of broad distribution. The spread of the peak is related to the specific position of interaction of the particle in the central hit pixel. Particles interacting in the middle of a pixel deposit a greater charge in the central hit pixel. Such events exhibit a cluster height value which is higher than that when the particles interact in the periphery of the hit pixel. The peak asymmetric shape towards lower energy accounts for the greater number of events interacting in the central pixel periphery than those interacting in the middle of the central pixel. The distribution over increasing sensor bias values shifts to higher energies due to the greater suppression of charge sharing and resulting increased greater energy collected by the central cluster height pixel.

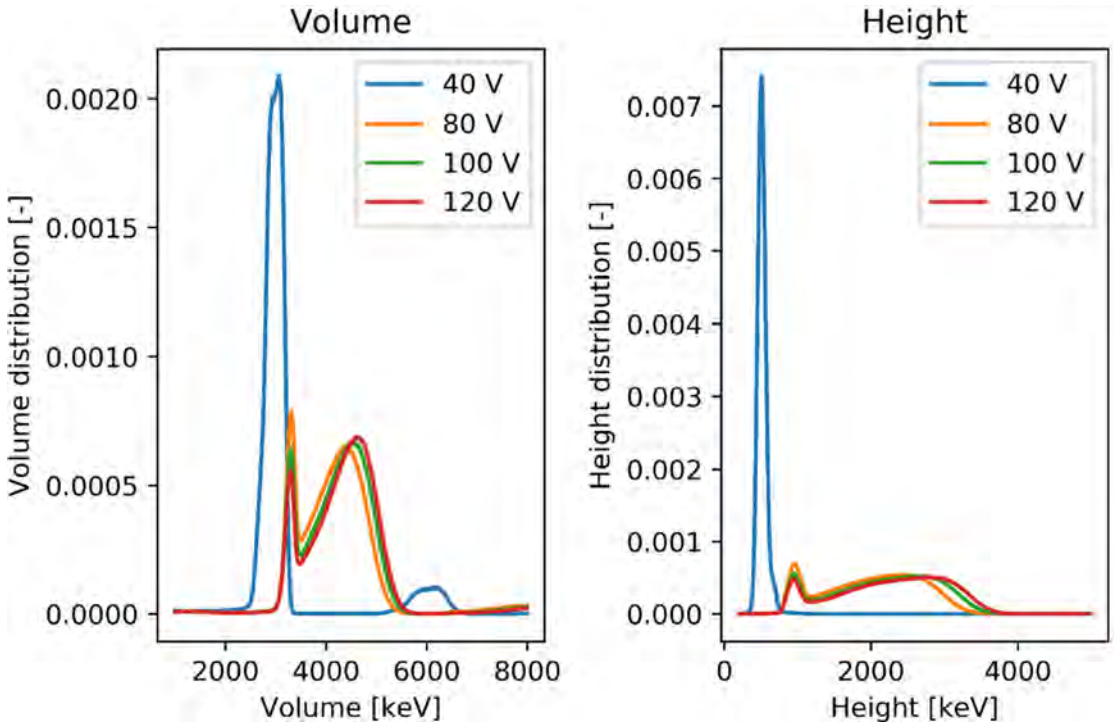

Fig. 16. Alpha particle deposited energy spectra (left) and cluster pixel height distribution (right). Data shown for one setting of source-to-detector distance (25 mm). Results shown were calibrated with the low-energy calibration [26]. Data are given for various bias sensor voltages (40, 80, 100, 120 V). Plot axis in linear scale.

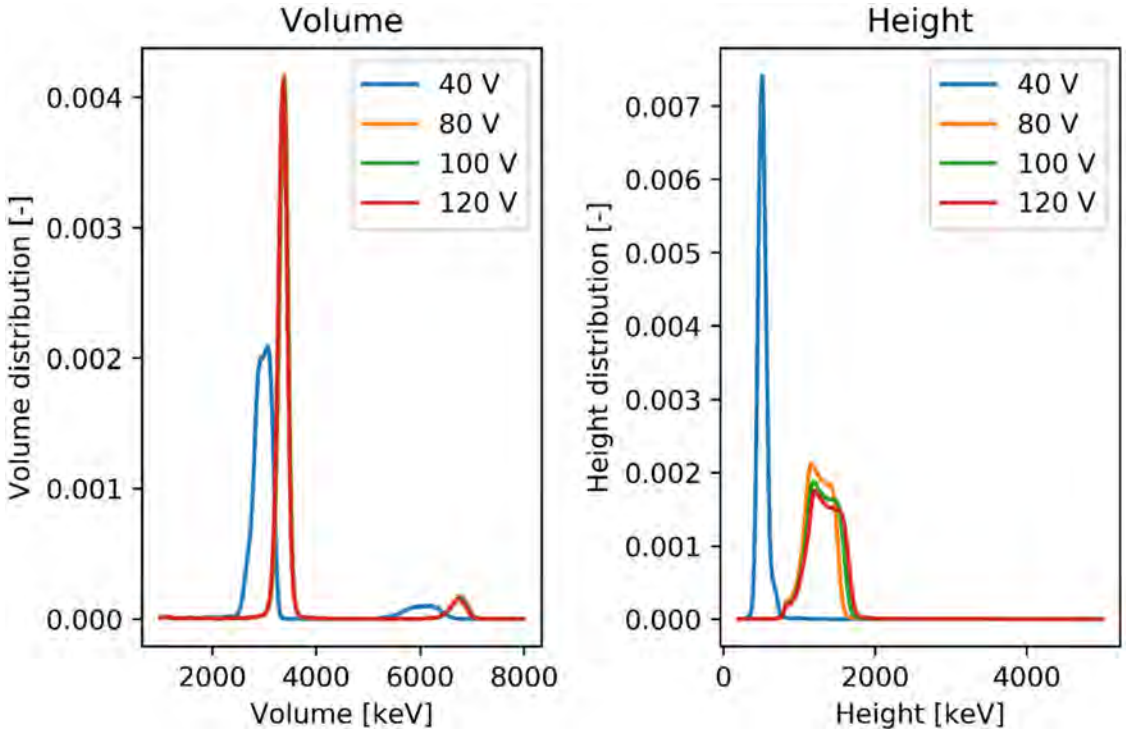

Fig. 17. Same as Fig. 16 using the new high-energy calibration.

5.3. Energy spread over the detector pixel matrix, alpha particles

The results and spectra presented were collected in one setting of sensor-to-detector distance and thus contain a spatial-dependent broadening due to the setup and geometry used. To evaluate this effect, we examined the distribution of values across the detector pixels.

The deposited energy of the alpha particles derived over the pixel matrix is shown in Fig. 18 for various bias sensor voltages (40, 80, 100, 120 V). The developed high-energy calibration is used. Events processed for this plot were filtered: only single isolated alpha particles were processed in the figures shown. The measured deposited energy is displayed in colour, the same value range scale applies for all plots. The same data were used in Fig. 17. The mean value of deposited energy

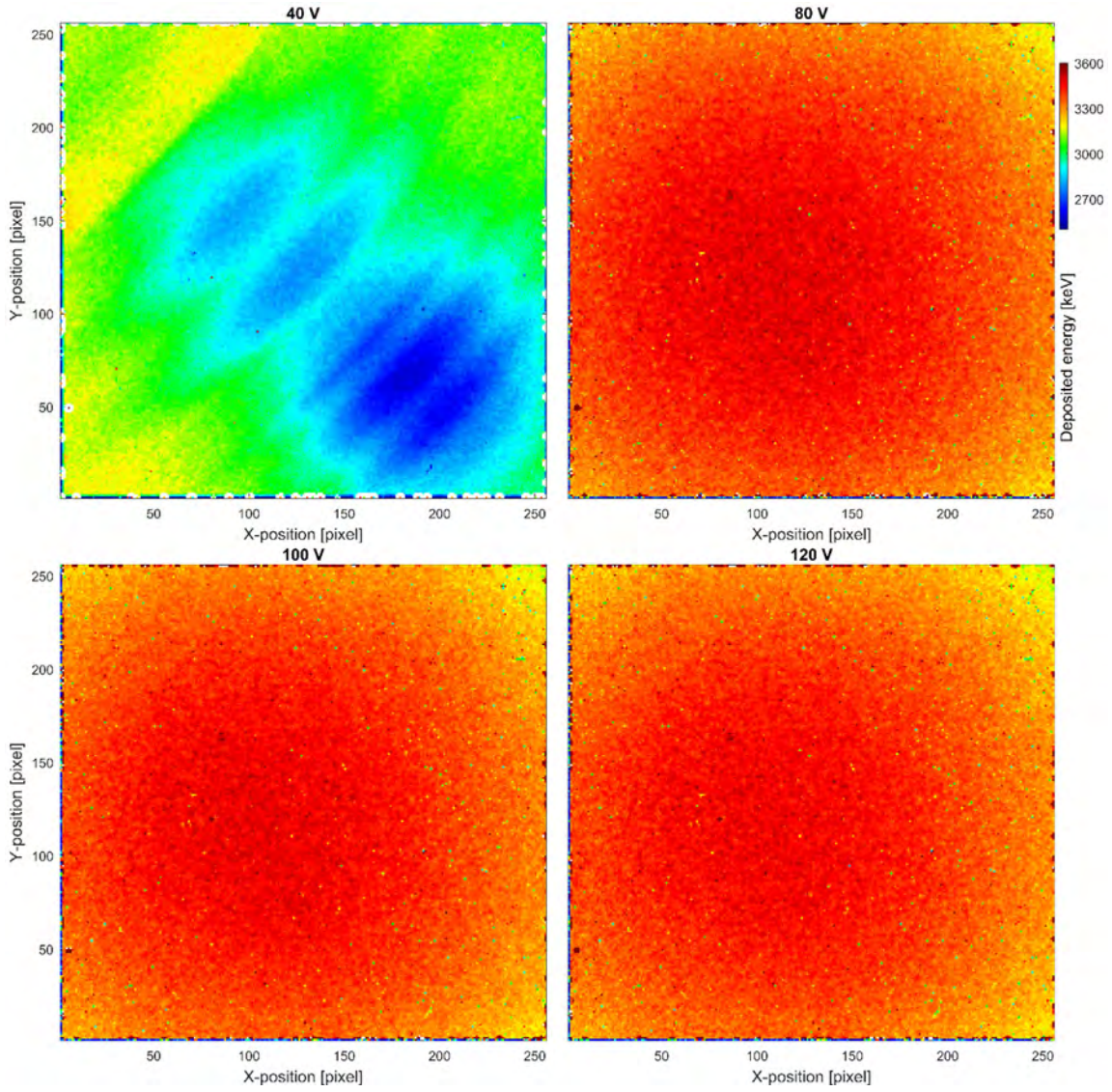

Fig. 18. Distribution of deposited energy (displayed in colour in [keV]) of alpha particles over the detector pixel matrix. Data used for one sensor-to-detector setting. The response is shown for different sensor bias: 40 V, 80 V, 100 V, 120 V – see plot headings. Data collected for one setting of source-to-detector distance (25 mm, same data from Fig. 17 left). The new high-energy calibration was applied. A radial energy spreading is visible due to the setup geometry.

is around 3.6 MeV which is reproduced by the high-bias data. Low bias data, such as the 40 V value used, results in an underestimation of the deposited energy. This is due to collection loss of the deposited charge in the partly depleted sensor volume. The shift is in the range of about 300 to 600 keV which is 10%–20% of the deposited energy. The spatially localized value gradients and patterns over the sensor matrix are due to inhomogeneity of the electric field which become manifest especially at low-bias non-depleted sensor settings [41]. The high bias data exhibit also a spatially dependent distribution with circular pattern of energy spread over the sensor pixel matrix. This results from a radially oriented spatial gradient due to the setup geometry used (Section 4.4). The source was placed perpendicular nearly to the centre of the detector (around pixel coordinates 150 × 150, visible on the high bias data). The energy spread results from the different energy loss of the alpha particles crossing different path lengths over the air distance and also across the target thin cover and the detector non-sensitive thin electrode (see Section 4.4). The broadening has an extent of few hundred keV (< 10%) and ranges from 3500 to 3200 keV.

The distribution of cluster pixel height over the pixel matrix is shown Fig. 19. Results are shown for the same data and bias sensor voltages (40, 80, 100, 120 V). The low-bias data yield an underestimation of the cluster pixel height. The shift is approximately 600 keV which is about 50% of the expected value of around 1200 keV which is registered in the high-bias data. The ring patterns visible correspond to spatial inhomogeneity in the electric field across the semiconductor sensor. The observed curved band patterns reflect and follow radial rings in the silicon crystal growth crystal [46].

5.4. Wide-range alpha particle data, multiplet events

The response over wide range can be examined by analysing the pile-up events in the alpha particle data collected from the ^{241}Am source. Multiplets such as doubles, triplets and higher order events can be registered, resolved and analysed. In Timepix detector, events arriving at the same (or partially overlapping) region within the acquisition time of the given detector data frame are registered as a single event. In such events, the per-pixel energy values of each event component in the multiplet are integrated (are added up). This produces multiplet values of deposited energy. The complete spectrum of deposited energy displayed in wide range is shown in Fig. 20 (left).

The deposited energy spectra contain besides the main component — the single alpha particle events and multiple event components. The Y axis is plotted in log scale. Several group events are resolved

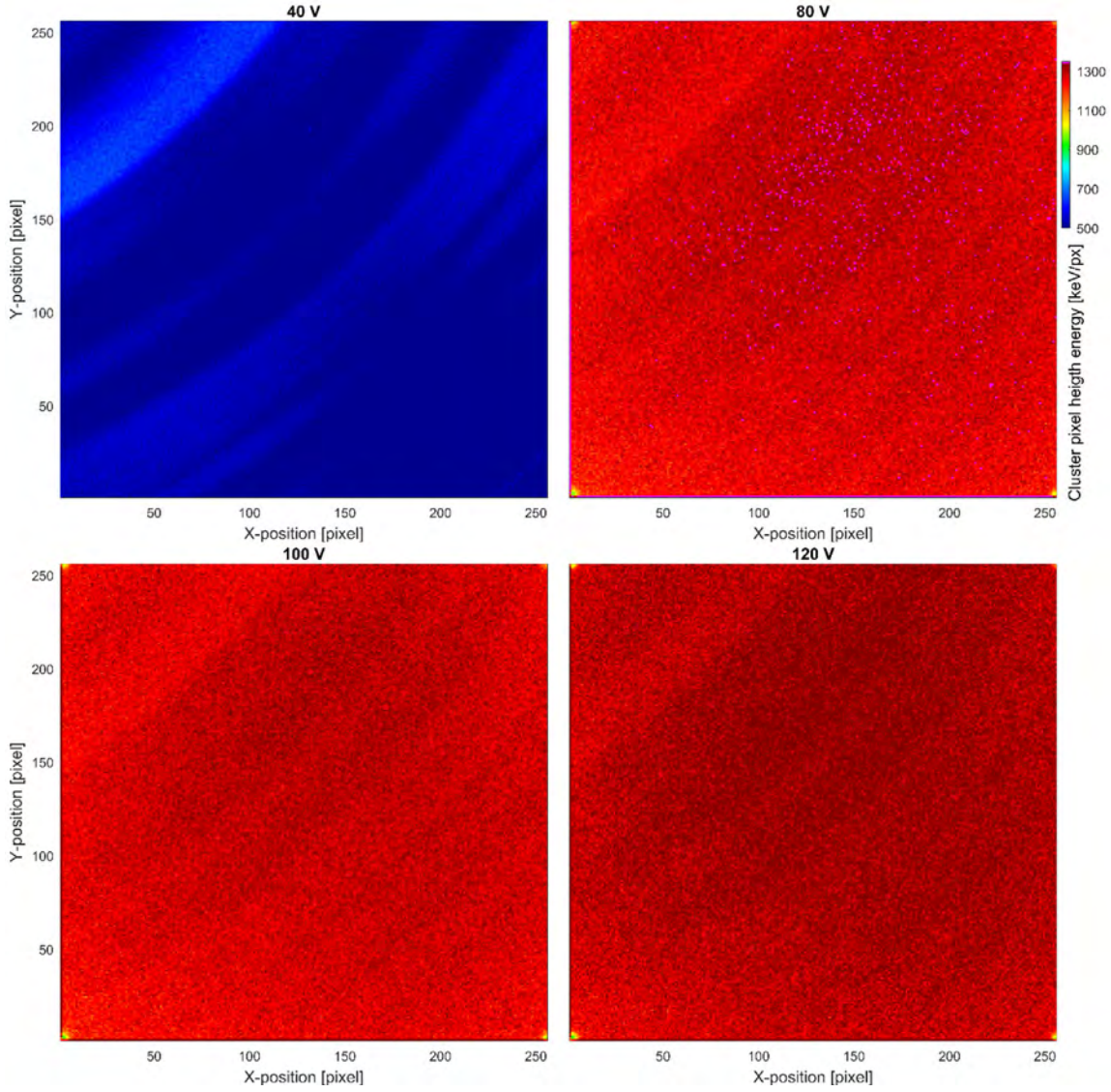

Fig. 19. Similar to Fig. 18 showing the spatial distribution of cluster height energy. Data shown for one source-to-distance (25 mm, same data from Fig. 17 right). The new high-energy calibration was applied.

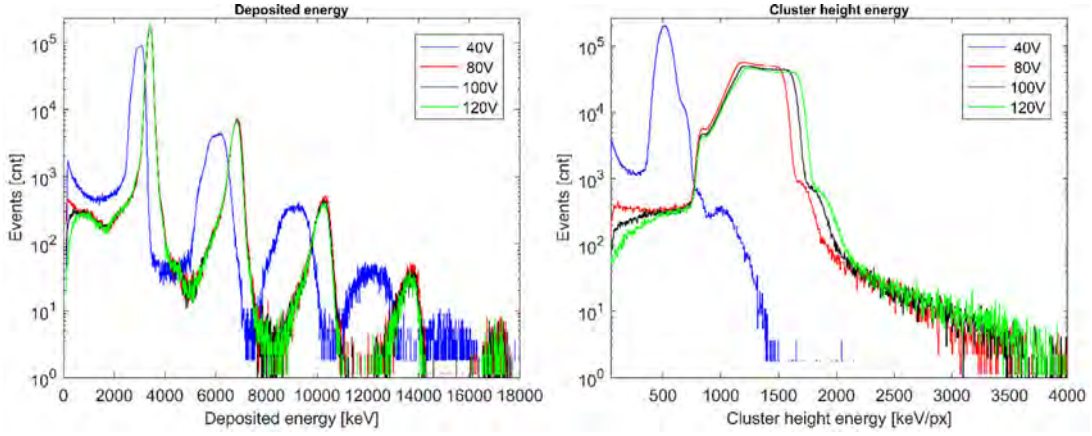

Fig. 20. Deposited energy spectra (left) and cluster height energy spectra (right) for the same data as in Figs. 16 and 17, respectively. The distributions are normalized for the same number of events. *Y* axis is set in log scale.

— up to 5-fold multiplet components (see the peaks above 4 MeV). In the low-bias data, the group components exhibit underestimated energy values which approximatively follow multiple factors of the single event group. The high-bias data yield correct values in the

proper factor sequence. The multiplet component peaks have maxima values at approximately the following sequence: 3.4 MeV (single event), 6.8 MeV (doublet), 10.2 MeV (triplet), 13.6 MeV (4 fold multiplet) and 17.0 MeV (5 fold multiplet). The components are broadened due to the source-to-detector settings and setup geometry.

The distribution of cluster pixel height is given in Fig. 20 (right). The cluster height distribution does not exhibit multiplet event groups. Doublet and higher multiplet events have two and more peaks in the sense of per-pixel height in the given multiplet cluster. However, just one height peak (the one with the highest energy) is evaluated and plotted in the cluster spectra (Figs. 17, 20 right).

5.5. 19 MeV protons

The high-energy per-pixel calibration was applied to protons. A high-energy primary 160 MeV proton beam was used from the ion synchrotron at HIMAC, Chiba. The same detector was used as above for the calibration (MiniPIX Timepix with a 300 μm silicon sensor). A beam energy degrader filter of 163.87 mm of water was used to lower the proton energy to approximately 19.4 MeV and LET of 4.8 keV/μm in silicon. This provides a deposited energy of 1440 keV in 300 μm of silicon (the detector was placed perpendicular to the beam). The deposited energy spectrum and cluster pixel height distribution are given in Fig. 21. Results given were processed with the low-energy calibration (blue) and the new high-energy calibration (red). According to the value range of the cluster pixel height of the registered event, the high-energy distributions consist of four region components: A+B, C, D, and undefined (see colour labels). The A+B component (green) shows clusters for which all pixels including the cluster pixel height are within the A+B region, i.e., below the T2 threshold border. i.e., in low-energy calibration. Component C (purple) shows events which have at least one cluster pixel in the C region i.e., above T2 and below T3 while the rest of the pixels are below T2. Component D (yellow) contains events with at least one pixel above T3 and below T4 and the rest of the pixels below T3. The undefined component (black) are clusters that are not included in any of the three components i.e., clusters with pixels that exceed the T4 threshold.

The resulting deposited energy spectrum using the high-energy calibration (red curve) yields a maximum at 1290 keV. The low-energy calibration yields a maximum at 1230 keV. The expected value is 1440 keV from model calculation. The broadening includes significant beam energy straggling across the beam filter (PMMA plate) and over the trajectory in air (few m). The results between both calibrations are approximately similar. The cluster height distribution corresponds to the high-energy regions C+D. The most probable deposited energy is higher for the high-energy calibration. The high-energy calibration has a reduced tail (events with energies larger than 2 MeV). With the application of the high-energy calibration, the most probable energy shifts from 1230 keV (low-energy calibration) to 1290 keV. Part of the difference between the theoretical deposited energy and the measured energy can be accounted for by large shift in the beam energy with the solid-state beam degrader. This is also due to the relatively low energy of the particles reaching the detector which approaches the Bragg's peak and is thus increasingly sensitive to fluctuations. The increased events in deposited energy in the main component, i.e., between 1–2 MeV in the high-energy calibration results, are due to the correct derivation of overestimated events above 2 MeV in the low-energy calibration results. Such events exhibit per-pixel height values in the C and D regions and yield, when only the low-energy calibration is used, overestimated values of deposited energy (see events in the blue curve above 2 MeV). A ToT per-pixel value in those high-energy regions, i.e., above the threshold border T3, predominantly yields an overestimated energy value when the low-energy calibration is extended i.e., linearly extrapolated, into the D region. The high-energy tail component is due to statistical fluctuations described by Landau distribution which is added to the doublet component at around 2.7 MeV which is about twice the energy of the single main component energy.

The height distributions exhibit a significant difference between the low-energy and high-energy calibrations. The low-energy calibration provides a lower-energy component of maxima just below 1 MeV and a high-energy broad component reaching over 4 MeV. The high-energy calibration results in a more localized distribution with a main component of maxima slightly above 1 MeV and a narrower high-energy component up to 2.5 MeV. Events with heights up to this range is derived from extrapolation of the quadratic function in region D into region E. Therefore, this *undefined component* is not precise. The corrected height distribution shows the same double peak formation as in the measurements with alpha particles from ^{241}Am source. The left peak low-energy component consists mainly of events in the A+B regions. The right high-energy broad component results from events in the C and D regions. Such pattern should be observed in general for individual monoenergetic charged particles. This effect and observed pattern (asymmetric broad peak for the high-energy component) results from the uneven distribution of deposited energy between the impact hit pixel and the adjacent pixels. This effect is determined by the spatial distribution and distance of the particle in the hit pixel from the pixel centre and the border pixels.

5.6. 400 MeV/u ^{12}C ions

Test measurements were carried out also with a 400 MeV/u ^{12}C beam at HIMAC using the same pixel detector MiniPIX Timepix with 300 μm silicon sensor. The registered deposited energy spectrum and cluster height distribution are given in Fig. 22. Results are shown for the low-energy (blue curve) and high-energy (red) calibrations. For the latter, events with cluster height energies in the region E i.e., above the high-energy threshold border T4, were processed with the extrapolated polynomic calibration function of region D. The components of the high-energy calibration are included and indicated (same processing and labels as in Fig. 21).

In the deposited energy spectrum, the expected value has maxima 6114 keV (from model calculation [47]). The results show a main component which appears as a broad peak between 3 and 6 MeV. The difference can be due to the extrapolation of the fitted function from the lower region D into the saturation region E of the spectral response at higher energy region around and above 2 MeV per pixel. A limited portion of events in the main carbon peak have cluster height values in region D which supports the application and partially justifies the extrapolation of the high-energy calibration. The discrepancy may be caused by the loss of unambiguity of the calibration curve between the regions D and E. Given the evolution of the calibration curve as illustrated in Fig. 1, at very high per-pixel energy i.e., region E and beyond, two possible energies can correspond to one ToT value. Therefore, we assume that for such carbon ions the deposited energy in the highest pixel was so large that it corresponds to region E but it was incorrectly assigned to region D. The broad component at higher energy, between 7 and 11 MeV includes contribution from these two main components with cluster height values in the saturated region E (label undefined in Fig. 22). This group includes also multiplet events i.e., doublet pairs of primary particle events which were registered and processed in the detector as a single event. The deposited energy spectrum using the low-energy spectrum gives overestimated and broadened values. This is given by the extrapolation of the linear region B and the resulting overestimation of the per-pixel energy above the linear region border (about 850 keV/px).

Measurements with carbon ions of the energy and setup used are accompanied by secondary products and charged particles produced from fragmentation reactions, see e.g., Ref. [48]. The kinetic energy of fragment ions is often near the energy of the original projectile. In the measurement performed, secondary fragments consist of H, He, Li, Be, and B ions which should deposit in the pixel detector energies of

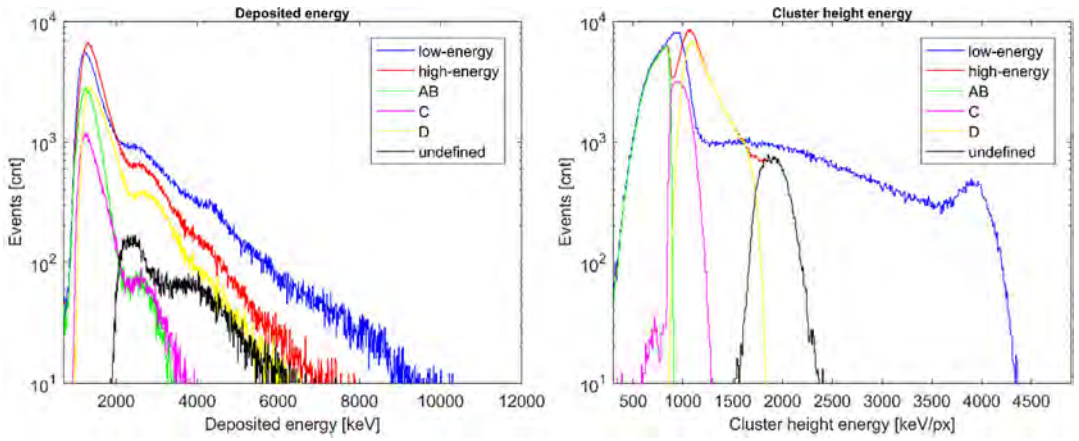

Fig. 21. Deposited energy spectrum (left) and cluster pixel height distribution (right) for 19.4 MeV protons. Measured at HIMAC, Chiba with the same MiniPIX Timepix detector with a 300 μm silicon sensor. In the figures all registered events are displayed, no event filtering was applied. Results shown were processed with the low-energy calibration (blue) and the new high-energy calibration (red). The high-energy data (red) consists of various components as indicated (colour labels described in inset). (For interpretation of the references to colour in this figure legend, the reader is referred to the web version of this article.)

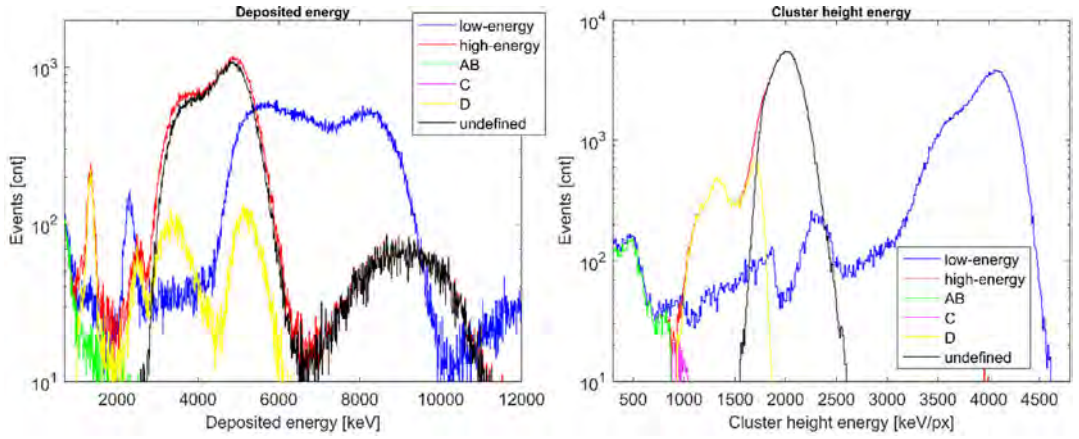

Fig. 22. Similar as Fig. 21 for 400 MeV/u ^{12}C ions. Data measured at the ion synchrotron in HIMAC, Chiba, with the same Timepix detector with a 300 μm thick silicon sensor. In the figures all registered events are displayed, no event filtering was applied.

180, 690, 1530, 2640, and 4140 keV, respectively. In the results with the high-energy calibration, it is possible to identify individual fragment components with approximatively correct energy assignments. The peaks with measured maxima at 1350 keV and 2490 keV correspond to the dominant Li and Be ion components. A sizeable part of the events contributing to these components correspond to the region D and are well resolved in the D region component (yellow curve in Fig. 22) of the deposited energy spectrum. Although the measured energy of Li and Be peaks are partly smaller than the theoretically calculated, this shows that the high-energy calibration can be successfully applied for light ions. The difference is partially caused by the reduced width of the sensor depleted volume because the sensor was operated at partly low bias (50 V). Such bias voltage is not sufficient for a full depleted region. Similar underestimation of deposited energies was obtained for H and He fragment ions in the spectrum. The B ion fragments are likely the part of the main carbon peak. Since most of the clusters in that peak are in undefined region the calculated deposited energy is not reliable. Nevertheless, there is a minority of clusters which belong to the D region. The clusters in D region form two peaks. One with energy of 3.5 MeV and the second one 5.2 MeV. We assume that the first one is created by B ions and the second one by primary C ions which might be incorrectly placed in the D region instead of E region.

Detection of ions, such as the ^{12}C ions used in this work, produce events with large cluster height values [41] which fall above the low-energy range (i.e., beyond region B) – see Fig. 22. The cluster height distribution contains events in the distorted region D and in the saturated undefined region E. The occupation in these regions is of varying extent increasing towards greater energy for increasingly heavier ions. For the ^{12}C ions used, region D has the minor component and region E has the greater component. Almost no events correspond to region C. This situation is unlike the proton data which has height events in the linear C region in addition also to regions D+E. The dominant component in the proton data is the region D. In the carbon data, on the contrary, most events correspond to region E (and partly also F) thus exceeding the high-energy calibration limit (above the T4 threshold border). The energy derivation above this range is performed also by of extrapolation of the calibration. Results are given in Fig. 22. The low-energy calibration, which for the high-energy regions is extrapolated throughout this work, produces greatly overestimated values of both cluster height and deposited energy. This is consequence of the extended extrapolation of the low-energy dependency, valid in region B, well into the high-energy regions C+D and also the well-distorted and saturated regions E+F.

5.7. Energy resolution

Evaluation of the energy resolution in the high-energy region is performed on deposited energy spectra of the measured data. In the alpha particles from the ^{241}Am source the data collected at 80 V yield a deposited energy distribution with peak maximum at 3420 keV and FWHM 210 keV which gives an energy resolution of 6.1%. The

achieved resolution includes broadening of the deposited energy in the range from about 3200 keV up to 3550 keV (see Fig. 18) due to the source-to-detector distance and geometry used.

In the proton data measured, the deposited energy spectrum has maximum 1290 keV, FWHM 495 keV yielding an energy resolution of 38%. This result includes the large shift and significant broadening in the proton energy from 160 MeV to 19 MeV done in the solid-state beam energy degrader.

In the light ion ^{12}C data measured, we evaluate well-defined components in the deposited energy spectra. The Li peak has maximum 1350 keV, FWHM 175 keV and energy resolution 13%. The Be peak has maximum 2535 keV, FWHM 540 keV and energy resolution 21%. The resulting resolution includes broadening of the deposited energy from the production of fragmentation reaction products and their trajectory in the beam degrader and in the air distance.

5.8. LET spectra, light ions

The granularity and spectral response of the Timepix detector enables to derive the linear-energy-transfer (LET) of charged particles [13,22–25]. The directional response is exploited to determine the particle LET in high-resolution and wide dynamic range [25]. The LET is derived as the ratio of the deposited energy and the particle track length across the sensor. The measurement of the deposited energy is essential, especially for high-energy loss particles such as light and heavy ions. The distortion and saturation of the per-pixel energy response can be in part compensated by exploiting the charge sharing effect. The extent of charge sharing is determined and can be adjusted by the sensor applied voltage (see Section 4.1).

In the work performed, the well-described range of energy response at the per-pixel level has been extended to around 1750 keV. This level is determined by the high-energy threshold border T4. This corresponds to about 4 MeV at the particle deposited energy level. This corresponds to a well-described maximum value of LET of 13.3 keV/um in silicon derived for the particles depositing 4 MeV through the 300 μm thick sensor used. This upper range can be examined in this work with the light ion data measured. The expected model-based LET values [47] of primary beam and reaction products from fragmentation 400 MeV/u ^{12}C data measured are: 20.0, 14.4, 8.8, 5.2, 2.3 and 0.57 keV/μm for the main components of corresponding 400 MeV/u energy ^{12}C, ^{10}B, ^{9}Be, ^{7}Li, ^{4}He ions and protons, respectively. The lower energy values fall within the range of the developed high-energy calibration. For $Z \geq 6$ ions as well as light ions of lower energy, at the level about $<$ 100 MeV/u, thus exhibiting increased energy loss, the detector spectral response strongly saturates and can no longer provide reliable LET values without further correction.

6. Conclusions, outlook

A high-energy calibration method has been developed for Timepix detectors with silicon sensors using alpha particles from a standard radioactive source in air. The new calibration enables to extend the spectral range at the detector pixel level up to 1.75 MeV/px which is double the range of the current low-energy calibration. The low-energy calibration is based on discrete low-energy X rays in the range 5–60 keV and is extrapolated over the linear range up to about 850 keV per-pixel. The new high-energy calibration describes the range above this level. Two high-energy regions are identified and described: a narrow region C of shifted linear dependence up to about 1.2 MeV/px, and a wide region D of quadratic dependence up to 1.75 MeV/px. The technique requires a basic setup and is designed to be as simple as possible being intended for wide-application and non-expert users. Measurements are performed in air with a simple geometry without collimators or foils within one day. It makes use of commonly available laboratory ^{241}Am alpha source of laboratory-level activity (kBq range). Data are collected at various sensor-to-distance values in the range 20–30 mm (six positions are optimal) and several applied bias values (about 4 values) in the range 70–150 V. The applied bias is a sensitive and key parameter which determines the extent of charge sharing in the detector sensor and is used to determine and tune the collected energy per-pixel. This is critical to vary and set the amount of collected charge especially for the central hit pixel, which collect most of the deposited charge, in the given cluster. This approach, combining and tuning the sensor-to-detector distance and the applied sensor bias, is exploited to deposit and adjust the deposited energy per-pixel in the detector in wide range. The energy resolution achieved is overall estimated at 5% FWHM. The resolution derived in the collected data ranges from 6% to 13% and 21% up to 38% for alpha particles, light ion components in the ^{12}C data, and protons, respectively. These values included large fluctuations and significant broadening in the particle energy due to the geometry and beam or source-setup settings.

The need and application of the high-energy calibration are essential to provide a correct evaluation of high-energy loss particles, especially heavy charged particles. The overestimation and error induced by application of the standard low-energy calibration are non-negligible and can become significant. Differences in the derived deposited energy spectra and cluster height can reach up to factor of 2 and 3.

Results obtained in high deposited energy per-pixel regions show good agreement with calibration curves from previous work — Ref's [29,30]. Those studies used elaborate setups requiring particle accelerators and well-defined energies of the particles. The high-energy calibration shows correct and accurate results when applied to alpha particles and protons. Similarly, light ion data show significantly improved results of deposited energy. A limitation is the contribution of events with cluster height values above the high-energy threshold border (around 1750 keV/px). This occurs for ions of increasing Z value and decreasing energy i.e. approaching the Bragg peak region. For middle- and heavy-mass ions e.g., at and above around ^{12}C, the increasingly higher per-pixel energy depositions become dominant and the applicability of the developed high-energy calibration becomes limited. Possible corrections and/or modelling are envisaged to help further in this task.

As next step we plan to calibrate additional devices and analyse the correlations and functions between different coefficients with the aim to estimate of high-energy coefficients solely based on the low-energy calibration. That would enable to calculate the extended calibration simply from the knowledge of the basic set of low-energy coefficients A1, B1, C1 and T1. Such estimation might be also beneficial for the pixels around the edge of the chip which cannot be calibrated by the high-energy calibration. Outlook of this work is the implementation of the high-energy calibration for Timepix3 ASICs. Timepix3 provides event-based readout which is faster than the frame readout of Timepix2 chips. This decreases the irradiation time. Also, higher activity alpha sources could be used. Lastly, with the knowledge of high-energy calibration coefficients and per-pixel spectral response regions we would like to develop an extended calibration and an extrapolated model to reach into the distorted and saturated regions E and F. The ^{241}Am source has alpha energy of 5.578 MeV which can be thus further exploited to reach per-pixel height values up to 4–5 MeV (vacuum measurements required).

CRediT authorship contribution statement

Marek Sommer: Conceptualization, Methodology, Visualization, Writing – review & editing. **Carlos Granja:** Conceptualization, Validation, Visualization, Writing – original draft. **Satoshi Kodaira:** Resources, Writing – review & editing. **Ondřej Ploc:** Supervision.

Declaration of competing interest

The authors declare that they have no known competing financial interests or personal relationships that could have appeared to influence the work reported in this paper.

Acknowledgements

Work by M.S. and O.P. was supported in the frame of the Operational Program EU Project CRREAT No. CZ.02.1.01/0.0/0.0/15_003/0000481. Work by CG was performed in the frame of Research Contract No. 4000130480/20/NL/GLC/hh by the European Space Agency. Results were tested using data collected at HIMAC, Japan, in the frame of Project No. H377.

References

[1] X. Llopart, R. Ballabriga, M. Campbell, Timepix, a 65 k programmable pixel readout chip for arrival time, energy and/or photon counting measurements, Nucl. Instrum. Methods Phys. Res. A 581 (2007) 485–494.
[2] E.H.M. Heijne, History and future of radiation imaging with single quantum processing pixel detectors, Radiat. Meas. 140 (2021) 106436.
[3] R. Ballabriga, M. Campbell, X. Llopart, X, ASIC developments for radiation imaging applications: The Medipix and Timepix family, Nucl. Instrum. Methods Phys. Res. A 878 (2018) 20–23.
[4] E.H.M. Heijne, R. Ballabriga, M. Campbell, et al., Measuring radiation environment in LHC or anywhere else, on your computer screen with Medipix, Nucl. Instrum. Methods Phys. Res. A 699 (2013) 198–204.
[5] J. Jakubek, Semiconductor pixel detectors and their applications in life sciences, J. Instrum. 4 (2009) P03013.
[6] J. Dudak, High-resolution X-ray imaging applications of hybrid-pixel photon counting detectors Timepix, Radiat. Meas. 137 (2020) 106409.
[7] J. Zemlicka, J. Jakubek, M. Kroupa, et al., Energy- and position-sensitive pixel detector Timepix for X-ray fluorescence imaging, Nucl. Instrum. Methods A 607 (2009) 202–204.
[8] J. Jakubek, T. Holy, S. Pospisil, et al., Pixel detectors for imaging with heavy charged particles, Nucl. Instrum. Methods A 591 (2008) 155–158.
[9] L. Pinsky, S. Pospisil, Timepix-based detectors in mixed-field charged-particle radiation dosimetry applications, Radiat. Meas. 138 (2020) 106229.
[10] C. Granja, J. Jakubek, M. Martisikova, et al., Dynamic range and resolving power of the Timepix detector to heavy charged particles, J. Instrum. 13 (2018) C11003.
[11] C. Granja, S. Pospisil, Quantum dosimetry and online visualization of X-ray and charged particle radiation in aircraft at operational flight altitudes with the pixel detector Timepix, Adv. Space Res. 54 (2014) 241–251.
[12] C. Granja, K. Kudela, J. Jakubek, et al., Directional detection of charged particles and cosmic rays with the miniaturized radiation camera MiniPIX Timepix, Nucl. Instrum. Methods A 911 (2018) 142–152.
[13] C. Granja, P. Krist, J. Jakubek, et al., Energy loss and online directional track visualization of fast electrons with the pixel detector Timepix, Radiat. Meas. 59 (2013) 245–261.
[14] S. George, C.T. Severino, E. Frojdh, et al., Measurement of an accelerator based mixed field with a Timepix detector, J. Instrum. 10 (2015) P03005.
[15] T. Gehrke, L. Burigo, G. Arico, et al., Energy deposition measurements of single H-1, He-4 and C-12 ions of therapeutic energies in a silicon pixel detector, J. Instrum. 12 (2017) P04025.
[16] M. Martisikova, T. Gehrke, S. Berke, et al., Helium ion beam imaging for image guided ion radiotherapy, Rad. Oncology 13 (2018) 109.
[17] N. Stoffle, L. Pinsky, M. Kroupa, et al., Timepix-based radiation environment monitor measurements aboard the international space station, Nucl. Instrum. Methods Phys. Res. A 782 (2015) 143–148.
[18] M. Kroupa, A. Bahadori, T.T. Campbell-Ricketts, et al., A semiconductor radiation imaging pixel detector for space radiation dosimetry, Life Sci. Space Res. 6 (2015) 69–78.
[19] C. Granja, S. Polansky, Z. Vykydal, A. Owens, et al., The SATRAM Timepix spacecraft payload in open space on board the Proba-V satellite for wide range radiation monitoring in LEO orbit, Planet. Space Sci. 125 (2016) 114–129.
[20] S. Gohl, B. Bergmann, C. Granja, et al., Measurement of particle directions in low earth orbit with a Timepix, J. Instrum. 11 (2016) C11023.
[21] T. Baca, M. Jilek, I. Vertat, et al., Timepix in LEO orbit onboard the VZLUSAT-1 nanosatellite: 1 year of space radiation dosimetry measurements, J. Instrum. 13 (2018) C11010.
[22] C. Granja, J. Jakubek, S. Polansky, et al., Resolving power of pixel detector Timepix for wide-range electron, proton and ion detection, Nucl. Instrum. Methods A 908 (2018) 60–71.
[23] S. Hoang, L. Pinsky, R. Vilalta, et al., LET estimation of heavy ion particles based on a Timepix-Based Si detector, in: Int. Conf. on Computing in High Energy and Nuclear Physics, J. Physics Conf. Series 296 (2012) 022023.
[24] O. Ploc, M. Sommer, A. Molokanov, et al., Intercomparison of LET spectra measured with Timepix and TECP in reference radiation field CERF, in: IEEE Aerospace Conference Proceedings, 2018.
[25] C. Granja, C. Oancea, J. Jakubek, et al., Wide-range tracking and LET-spectra of energetic light and heavy charged particles, Nucl. Instrum. Methods A 988 (2021) 164901.
[26] J. Jakubek, Precise energy calibration of pixel detector working in time-over-threshold mode, Nucl. Instrum. Methods Phys. Res. A 633 (2011) S262–S266.
[27] D. Turecek, J. Jakubek, M. Kroupa, et al., Energy calibration of pixel detector working in time-over-threshold mode using test pulses, in: IEEE NSS Conf. Proc, 2011.
[28] M. Kroupa, J. Jakubek, P. Soukup, Optimization of the spectroscopic response of the Timepix detector, J. Instrum. 7 (2012) C02058.
[29] S.P. George, M. Kroupa, S. Wheeler, et al., Very high energy calibration of silicon Timepix detectors, J. Instrum. 13 (2018) P11014.
[30] M. Kroupa, T. Campbell-Ricketts, A. Bahadori, et al., Techniques for precise energy calibration of pixel particle detectors, Rev. Sci. Instrum. 88 (2017) 033301.
[31] M. Holik, G. Ahmadov, J. Broulim, et al., Alpha calibration of the Timepix pixel detector exploiting energy information gained from a common electrode signal, J. Instrum. 14 (2019) C06022.
[32] D. Turecek, J. Jakubek, P. Soukup, USB 3.0 readout and time-walk correction method for Timepix3 detector, J. Instrum. 11 (2016) C12065.
[33] D. Turecek, J. Jakubek, PIXET Software Package Tool for Control, Readout and Online Display of Pixel Detectors Medipix/Timepix, Advacam, Prague, 2015.
[34] Z. Vykydal, S. Pospisil, J. Jakubek, A portable pixel detector operating as an active nuclear emulsion and its application for X-ray and neutron tomography, in: Proc. 9th ICATPP Conf., 2006, pp. 779-784.
[35] B. Bergmann, M. Pichotka, S. Pospisil, et al., 3d track reconstruction capability of a silicon hybrid active pixel detector, Eur. Phys. J. C77 (2017) 421.
[36] K. Akiba, M. Artuso, R. Badman, et al., Charged particle tracking with the timepix asic, Nucl. Instrum. Methods Phys. Res. A 661 (2012) 31–49.
[37] M. Campbell, V. Havranek, E. Heijne, et al., Charge collection from proton and alpha particle tracks in silicon pixel detector devices, in: Proc. IEEE Nucl. Sci. Symp. and Med. Imag. Conf. Record, Honolulu, USA, 2007, pp. 1047–1050.
[38] J. Bouchami, A. Gutierrez, A. Houdayer, et al., Study of the charge sharing in silicon pixel detector with heavy ionizing particles interacting with a Medipix2 and a Timepix devices, in: Proc. IEEE Nucl. Sci. Symp. and Med. Imag. Conf. Record, Dresden, Germany, 2009.
[39] M. Platkevic, P. Cermak, J. Jakubek, et al., Characterization of charge collection in various semiconductor sensors with energetic protons and Timepix device, in: IEEE Nucl. Sci. Symp. and Medical Imaging Conf. Proc, 2011, pp. 4715-4719.
[40] M. Kroupa, S. Hoang, N. Stoffle, et al., Energy resolution and power consumption of Timepix detector for different detector settings and saturation of front-end electronics, J. Instrum. 9 (2014) C05008.
[41] C. Granja, J. Jakubek, U. Koester, et al., Response of the pixel detector Timepix to heavy ions, Nucl. Instrum. Methods A 633 (2011) S198–S202.
[42] S. Hoang, R. Vilalta, L. Pinsky, et al., Data analysis of tracks of heavy ion particles in Timepix detector, J. Phys. Conf. Ser. 523 (2014) 12.
[43] T. Campbell-Ricketts, M. Kroupa, L. Pinsky, Spectroscopy of high-energy ions with timepix3, J. Instrum. 11 (2016) P11007.
[44] S.M. Abu Al Azm, G. Chelkov, D. Kozhevnikov, et al., Response of timepix detector with GaAs:Cr and Si sensor to heavy ions, Phys. Part. Nuclei Lett. 13 (2016) 363–369.
[45] M. Kroupa, J. Jakubek, F. Krejci, Charge collection characterization with semiconductor pixel detector Timepix, in: Proc. IEEE Nucl. Sci. Symp. and Med. Imag. Conf. Record, Dresden, Germany, 2009, pp. 5066-5069.
[46] C. Granja, J. Jakubek, S. Pospisil, et al., Position-sensitive spectroscopy of ^{252}Cf fission fragments, Nucl. Instrum. Methods A 574 (2007) 472.
[47] J.F. Ziegler, M.D. Ziegler, J.P. Biersack, SRIM – The stopping and range of ions in matter, Nucl. Instrum. Methods Phys. Res. A 268 (2010) 1818–1823.
[48] N. Matsufuji, A. Fukurama, M. Komori, et al., Influences of fragment reaction of relativistic heavy charged particles on heavy-ion radiotherapy, Phys. Med. Biol. 48 (2003) 1605–1623.